Chapter 3: $NiCo_2O_4$/NiO/rGO as non-precious metal-based anode catalyst for methanol oxidation

3.1 Introduction

Conventional Pt-based electrocatalysts are difficult to commercialize because of their unavailability, high cost, and activity loss due to catalyst poisoning [1, 2, 3]. Conversely, non-noble metals and their oxides have been playing significant role in DMFC research as they may be potential replacement to the Pt-based catalysts. Easy availability, better electrochemical stability and low cost of transition metal oxides (TMOs) make them potential contenders of the noble-metal based anode catalysts [4]. The electrochemical characteristics of TMOs are enhanced by various redox sites provided by the varying oxidation states of transition metal ions [5]. Additionally, TMOs provide superior stability in alkaline media, surpassing the performance of noble-metal based catalysts in acidic media [2, 6, 7]. The performance of DMFC is basically dependent on the catalytic activity of the catalyst, rate of electron/ion transport within the catalyst and the interface between catalyst and electrolyte [8]. Among the plethora of TMOs, Co_3O_4 is a promising non-precious metal electrocatalyst on account of its better reversibility, stability, eco-friendliness, and cost-effectiveness [9, 10]. Moreover, NiO is gaining attention as a potential material for energy conversion/storage devices, because of its high pseudocapacitive properties and low oxidation potential [11]. However, low electron transfer rate and slow catalysis of these monometallic TMOs restrain their further development [12, 13]. Mixed transition metal oxides can overcome this due to the presence of more than one metal cations exhibiting reversible electron transfer. Additionally, they have enhanced electrical conductivity and rich redox reactions due to the presence of two distinct metal cations [13]. One such mixed metal oxide is $NiCo_2O_4$, which is formed by substituting Co atom by Ni in Co_3O_4. It has spinel structure, in which Ni^{2+} ions occupy octahedral sites and Co^{3+} occupy both octahedral and tetrahedral sites. It exhibits better electrochemical activity because of its higher thermodynamic stability and electronic conductivity, which is two-fold that of Co_3O_4 and NiO [13-16]. Various structural alterations, such as the use of carbon-based support materials, varied morphologies facilitating electron transfer, and induction of porosity, can further boost the electrical conductivity and exposure of active sites of TMOs [16, 17]. Composites having different crystalline phases can induce extra charges at the interface, which leads

to enhanced charge transport. For instance, it is found that the capacitance of nickel cobaltite ($NiCo_2O_4$) increases by inducing secondary phase NiO, which enriches the interfacial charge, thereby facilitating more redox reactions [16]. Various morphologies of $NiCo_2O_4$, such as nanoplates [18], nanowires [19], micro/nano spheres [20], etc. have also been employed in different conversion and storage devices. For instance, $NiCo_2O_4$ with various morphologies have been investigated for oxygen evolution reaction activity [21]. These nanosheets on subjection to 1.63V potential against reversible hydrogen electrode (RHE) in 1 M KOH can provide current density of 10 mA/cm^2 [22]. In order to enhance the surface area, inner cavities and active sites, several hollow architectures, including hollow spheres [23], yolk-shell hollow spheres [24], and others, are being investigated. Nevertheless, the conductivity of metal oxides cannot compete with the carbonaceous materials. Graphene is superior to other carbonaceous materials in terms of conductivity, surface area, rigidity, and chemical stability. $NiCo_2O_4$ nanosheets coated on CNTs offer much greater electrocatalytic activity than pristine $NiCo_2O_4$ [25]. Two-dimensional morphology of $NiCo_2O_4$ with a high concentration of active sites can operate as an effective OER reaction catalyst [21]. Au-$NiCo_2O_4$ supported on graphene sheet enhances the specific surface area and contributes to improved conductivity of $NiCo_2O_4$ [26]. Graphene and its various derivatives carry great potential in energy storage devices [27]. Among these derivatives, reduced graphene oxide (rGO) is remarkable because of its hydrophilicity, which is provided by oxygen-containing functional groups, such as hydroxyl, epoxy and carboxyl. Combination of conductivity and hydrophilicity renders rGO great potential as catalyst support for methanol oxidation. However, restacking lessens its practical implications [3, 27]. By creating its heterostructures with other nanostructures, restacking issues can be resolved.

In this chapter, layer-on-layer structure of binary mixed metal oxide, $NiCo_2O_4$/NiO is developed with rGO to form a porous nanocomposite. Secondary phase NiO is conjugated with $NiCo_2O_4$ to create additional active sites at the interface. The porous non-noble metal based nanocomposite (CNOG) endowed by layer-on-layer structure acts as a versatile electrode for methanol oxidation and supercapacitor. The key advantages of the nanocomposite are as follows: (i) Less aggregation of the metal oxides lead to effective use of the active sites; (ii) Enlarged surface area of the nanocomposite; (iii) Minimal restacking of rGO nanosheets; (iv) More electrode-electrolyte interactions due to enhanced surface area; (v) Mesopores on the electrode make it easier for

electrolyte ions to penetrate into the electrode; (vi) Non-noble metals lessen CO poisoning of the catalyst during methanol oxidation; and (vii) Increased conductivity of the nanocomposite due to presence of rGO. Hence, endowed by these improved properties, CNOG acts as a versatile electroactive material for catalysis of methanol oxidation reaction and supercapacitor electrode.

The supercapacitor application of CNOG will be discussed in chapter 5.

3.2 Experimental section

3.2.1 Material synthesis

3.2.1.1 Synthesis of $NiCo_2O_4$/NiO (CNO): In a 100 ml solution of DI water and ethanol, 1 mmol of $Co(NO_3)_2.6H_2O$ (Merck) and 2 mmol of $Ni(NO_3)_2.6H_2O$ (Merck) were dissolved. After stirring for some time, hexamethylenetetramine (6 mmol) was added to the above solution. After obtaining a homogeneous solution, the solution was heated in an autoclave at 120 °C for 18 hours. Following the washing process the sample was dried at 60°C. The dried powder was then annealed at 600 °C in air for 2 hours. Conversely, $NiCo_2O_4$ (NCO) was synthesized by using Co:Ni precursor in 2:1 molar ratio with annealing conditions being 350 °C for 2 hours.

3.2.1.2 Synthesis of $NiCo_2O_4$/NiO/rGO (CNOG): Graphite oxide was synthesised using improved Hummer's method [28]. To exfoliate graphite oxide, 20 mg of graphite oxide was dispersed in 40 ml of ethanol and sonicated. A solution containing 1.8 mmol of hexamethylene tetramine, 0.48 mmol of trisodium citrate, 2 mmol of nickel nitrate hexahydrate, and 1 mmol of cobalt nitrate hexahydrate was made in DI water. Both the solutions were mixed thoroughly and autoclaved at 120 °C for 18 hrs. The sample obtained after washing was dried and the powder obtained thereafter was annealed at 600°C to obtain CNOG. The heat treatment reduces graphene oxide (GO) to form reduced graphene oxide (rGO).

3.2.2 Material characterizations:

The structural characterizations of the samples were accomplished using X-ray diffractometer (XRD) Model D8, Make-Bruker Axs, Germany Focus, Fourier Transform Infrared Spectrometer (FTIR) (Model Frontier MIR FIR) in 400-4000 cm^{-1} range, and X-Ray Photoelectron Spectrometer (XPS)- Model ESCALAB Xi^+ of Thermo Fisher Scientific Pvt. Ltd., UK. Field emission scanning electron microscopy (FESEM) (Carl Zeiss Microscopy, Germany, Model Zeiss, Sigma) and transmission electron microscopy

(TEM) (TECNAI G2 20 S-TWIN (200KV)) were used for the morphological characterizations. The elemental composition of the prepared samples was evaluated using energy-dispersive X-Ray spectrometer JEOL, JAPAN of make JSM 6390LV. Pore analysis and Brunauer-Emmett-Teller surface area measurements were made using Autosorb iQ MP-AG (2 STAT) by Anton Paar.

3.2.3 Electrochemical characterizations:

Electrochemical studies were conducted using three-electrode set up in Gamry (Model-Gamry Interface 1010 E) at ambient environment. The set-up of the three-electrode system is: Pt wire (counter electrode), Ag/AgCl (reference electrode) and glassy carbon electrode coated with prepared active material (working electrode). The catalyst slurry was prepared by mixing the active material: carbon black: nafion in 75: 15: 10 ratios in isopropanol and water. The working electrodes were prepared by coating the catalyst slurry on Glassy Carbon Electrode (GCE) (5 mm) and dried at room temperature. Active material deposited was measured to be 0.1 mg. Prior to drop casting, GCEs were washed by DI water followed by alumina suspension. They were allowed to air dry after being rewashed in distilled water. 0.5 M NaOH was the supporting electrolyte in all electrochemical characterizations of the fuel cell. Cyclic voltammetry (CV), chronoamperometry (CA), and electrochemical impedance spectroscopy (EIS) were performed. The parameters considered were: - Potential window: -0.2 to 0.65 V; CA at 0.65 V for 1 hr; EIS 0.1 Hz-1 MHz with constant amplitude of 10 mV.

3.3 Results and Discussion

3.3.1 Morphological characterizations

The layered stacks of NCO nanoflakes are evident from the FESEM images shown in fig. 3.1a, and 3.1b. TEM images of NCO (shown in fig. 3.1c and 3.1d) corroborate well with the FESEM images. The SAED pattern in fig. 3.1e reveals the formation of different crystalline planes of NCO, as it consists of different planes (220), (311), (440) planes of $NiCo_2O_4$ with calculated d-spacing 0.294, 0.248, 0.147 nm respectively [29, 15, 17]. The morphology of CNO is presented in fig. 3.2 and fig. 3.3. CNO consists of $NiCo_2O_4$ nanoflakes and NiO nanoparticles, which adhere to one another to form chain like structures, as confirmed by the FESEM images in fig. 3.2a, 3.2b.

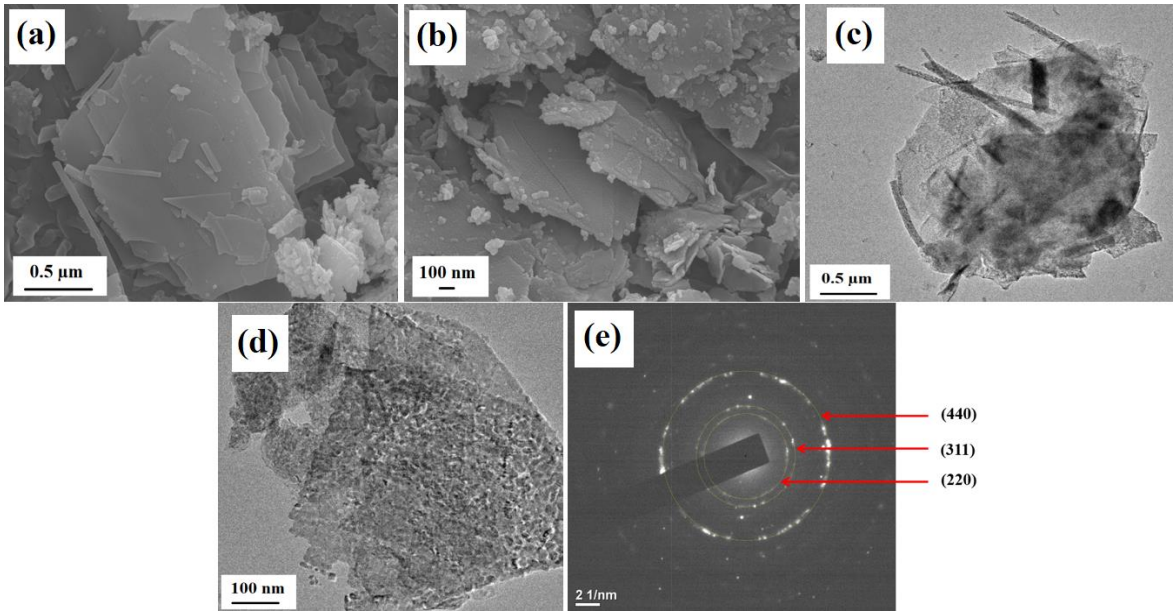

Figure 3.1: Morphology of NCO: (a), (b) FESEM images, (c), (d) TEM images, (e) SAED pattern

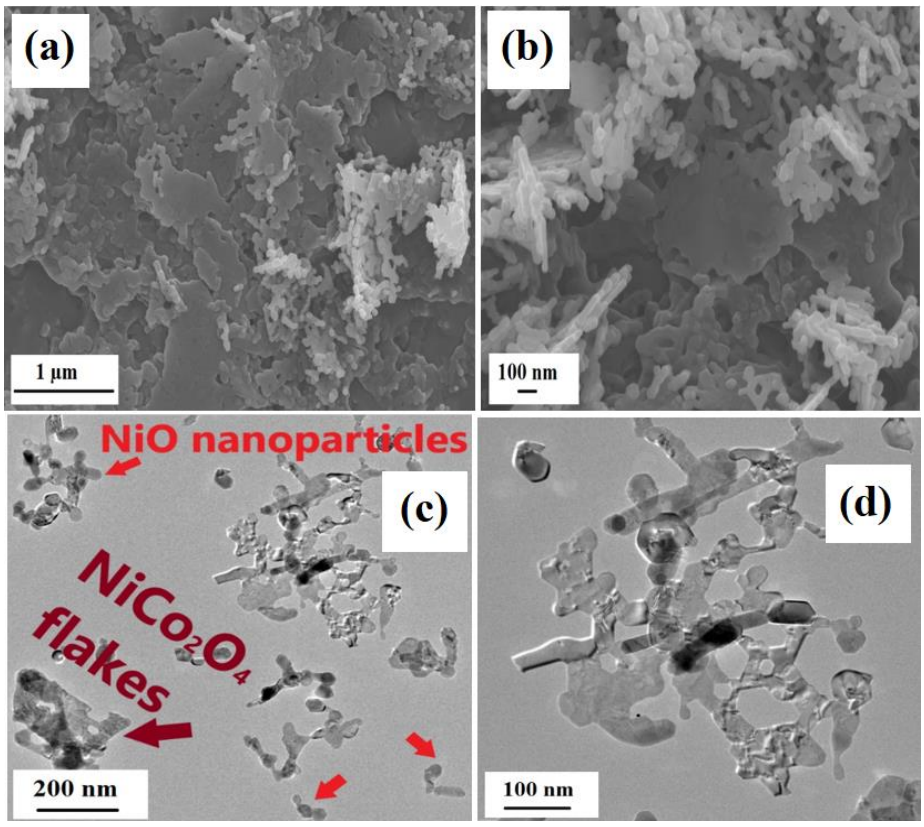

Figure 3.2: Morphology of CNO: (a), (b) FESEM images, (c)-(d) TEM images

The morphology of CNO is further established from the TEM images displayed in fig. 3.2c and 3.2d. The lattice planes depicted in fig. 3.3a and 3.3b correspond to (511) plane of NiO and (642) plane of $NiCo_2O_4$ respectively, thus confirming the formation of NiO and $NiCo_2O_4$. The SAED pattern in fig. 3.3c further affirms the formation of both phases i.e., NiO and $NiCo_2O_4$ as the SAED consists of different rings suggesting the planes (220), (422), (440), (622), (642) planes of $NiCo_2O_4$ with calculated d-spacing 0.292, 0.169, 0.148, 0.124, 0.110 nm respectively [29, 15, 17], and (331), (422), (511) planes of NiO with d-spacing 0.094, 0.087, 0.07 nm respectively [15].

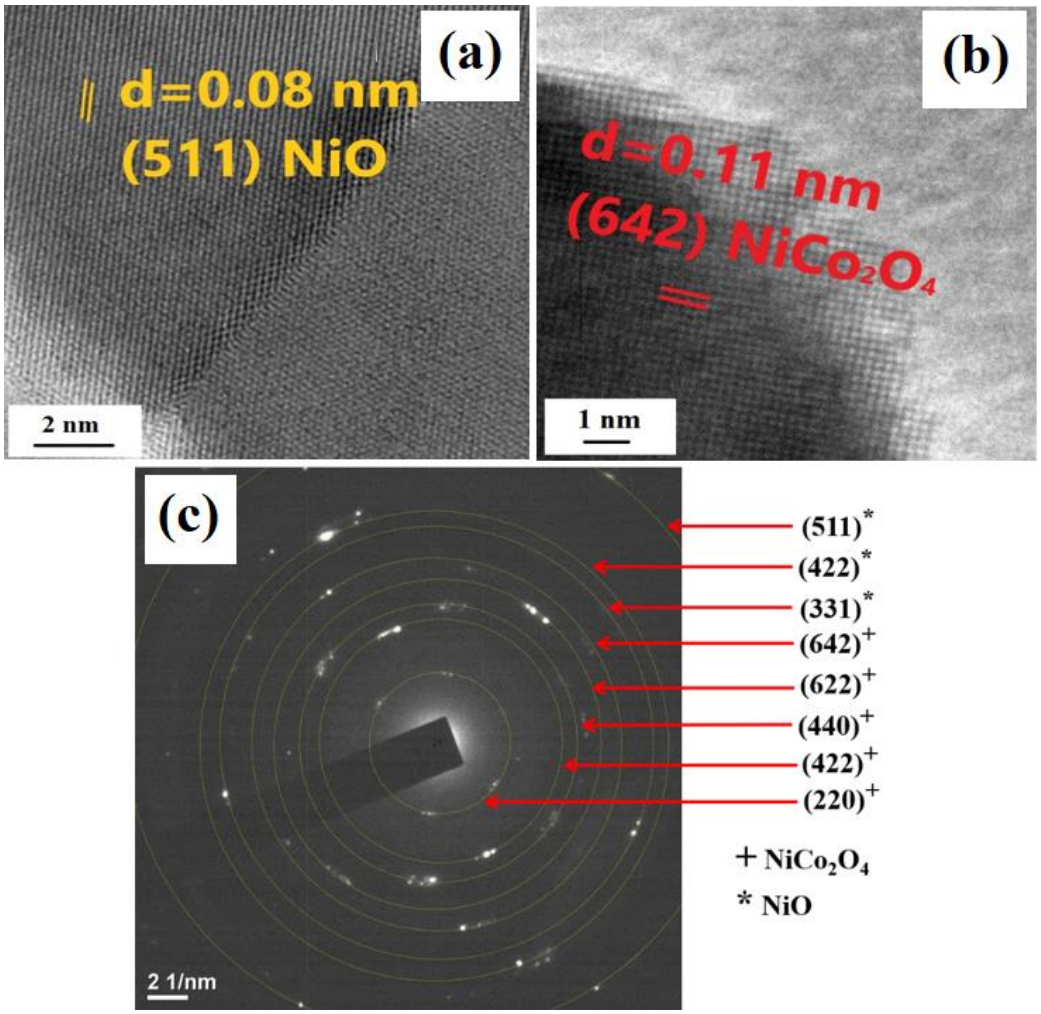

Figure 3.3: Morphology of CNO: (a)-(b) TEM images, (c) SAED pattern

The FESEM images (fig. 3.4a, 3.4b) of hybrid CNOG proves the presence of layered structure of $NiCo_2O_4$ nanoflakes and rGO nanosheets in which NiO nanoparticles stick together to form chain-like structures. The layer-on-layer structure of $NiCo_2O_4$ nanoflakes and rGO nanosheets can also be observed from the TEM images of CNOG in

fig. 3.4c and 3.4d. As can be observed from the fig. 3.4c, NiO nanoparticles are dispersed on the layer-on-layer structure of $NiCo_2O$ and rGO. In-situ growth of $NiCo_2O_4$/NiO on GO nanosheets, leads to the formation of spherical NiO nanoparticles. As seen in fig. 3.5a, these NiO nanoparticles adhere to one another to create an interconnected porous network. The -OH group of the NiO precursor, $Ni(OH)_2$ develops strong bond with the oxygen rich surface functional groups of GO, thus restricting the formation of NiO nanosheets, and favouring the formation of NiO nanoparticles [30].

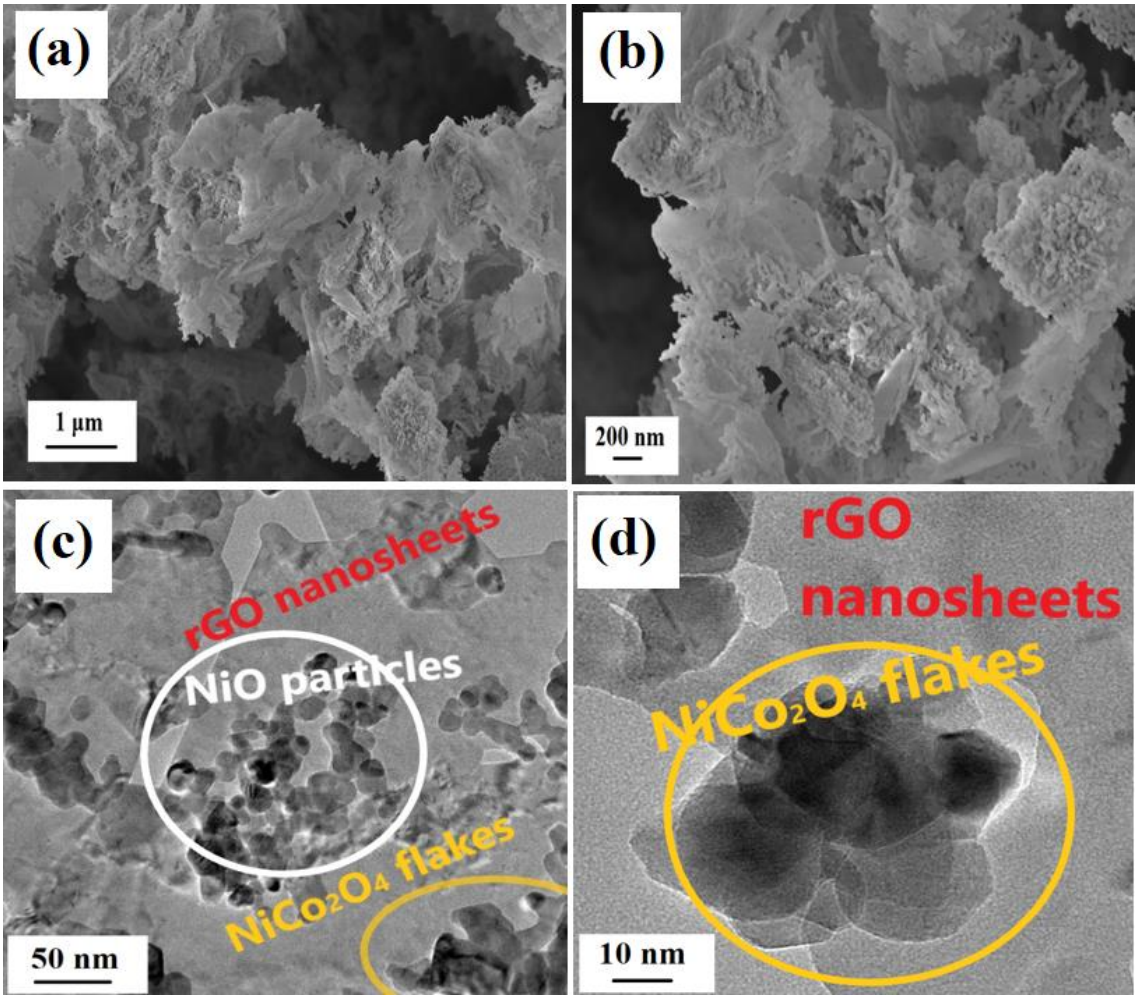

Figure 3.4: Morphology of CNOG: (a), (b)- FESEM images, (c)-(d) TEM images.

The HRTEM image of the NiO porous network in CNOG is displayed in fig. 3.5b. The region indicated by the yellow circle in fig. 3.5b is enlarged to reveal the lattice fringes shown in fig. 3.5c. The lattice fringes correspond to (511) plane of NiO with d-spacing of 0.08 nm. The layered stack of $NiCo_2O_4$ nanoflakes (marked by red and yellow circles)

in fig. 3.6a are enlarged in fig. 3.6b and 3.6c respectively. The d-spacing of 0.207 and 0.237 nm correspond to (400) and (222) plane of $NiCo_2O_4$ respectively. The selected area electron diffraction pattern in fig. 3.6d displays the presence of lattice planes (311), (400), (511), (533) of $NiCo_2O_4$, and (331), (511) of NiO. The energy-dispersive X-Ray spectroscopy (shown in fig. 3.7) and elemental mapping (in fig. 3.8) of CNOG confirms the uniform distribution of the elements Co, Ni, C and O throughout the structure.

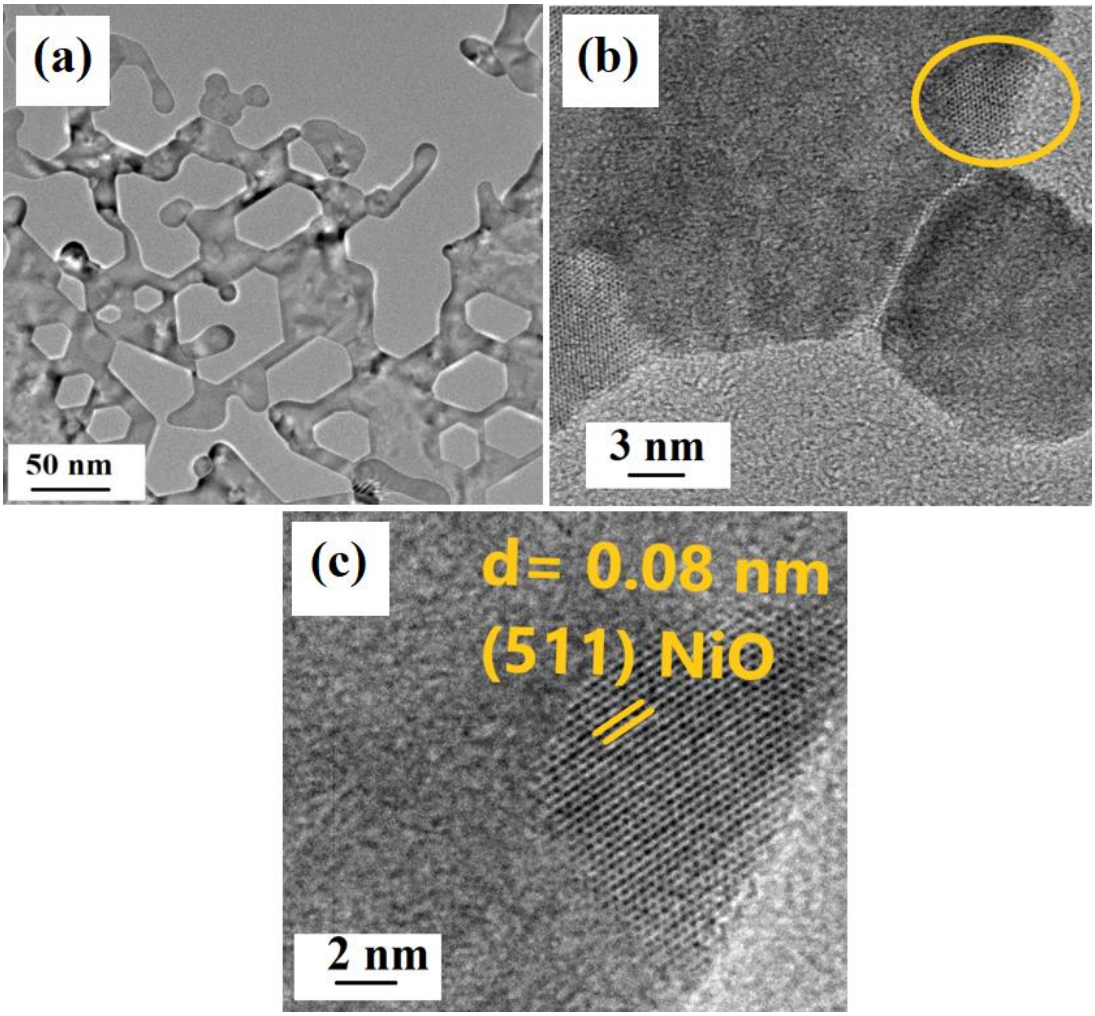

Figure 3.5: Morphology of CNOG: (a)-(c) TEM images. Yellow circle in fig. 3.5b is representing the area magnified in fig. 3.5c

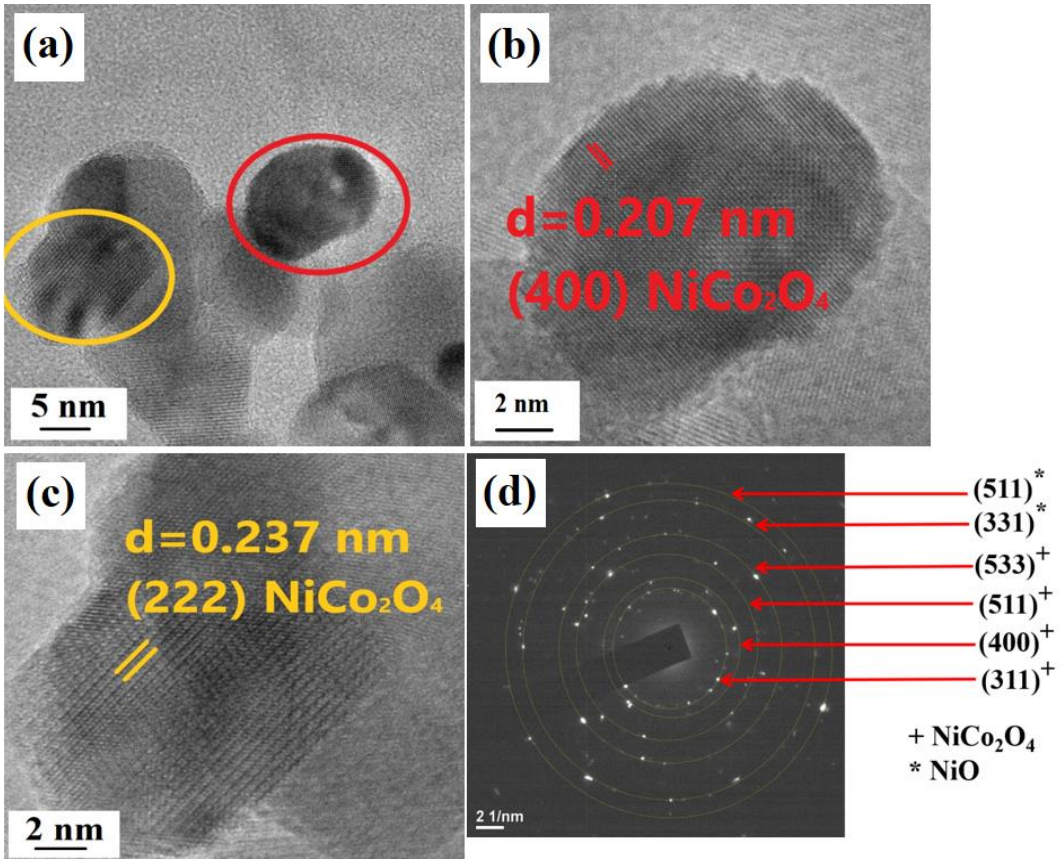

Figure 3.6: Morphology of CNOG: (a)-(c) TEM images. Red and yellow circles in fig. 3.6a are representing the area magnified in fig. 3.6b and 3.6c respectively, (d) SAED pattern

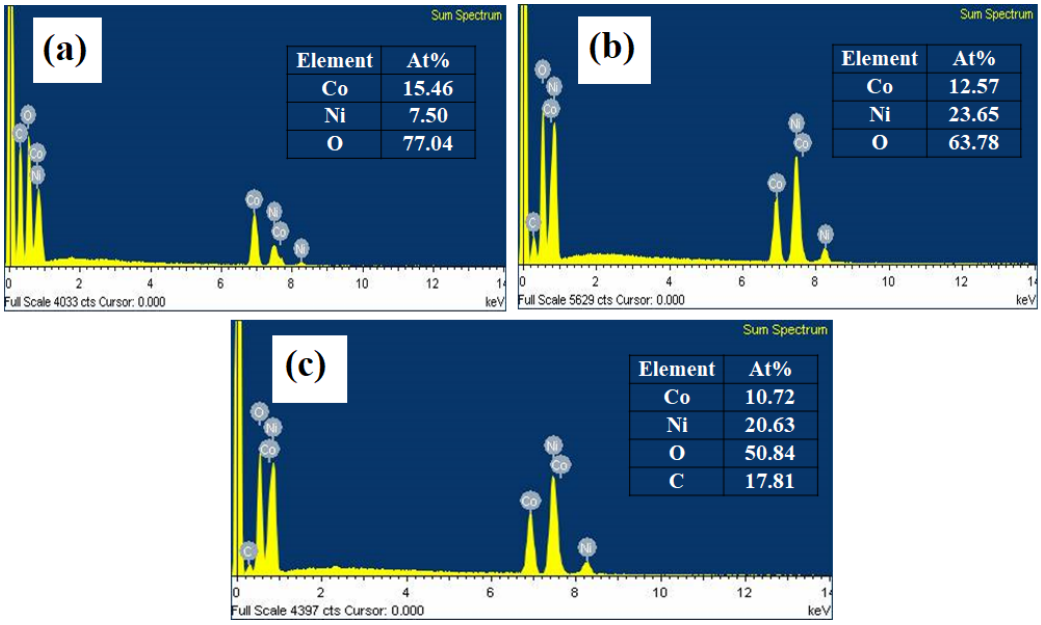

Figure 3.7: EDX spectra of NCO, CNO, and CNOG

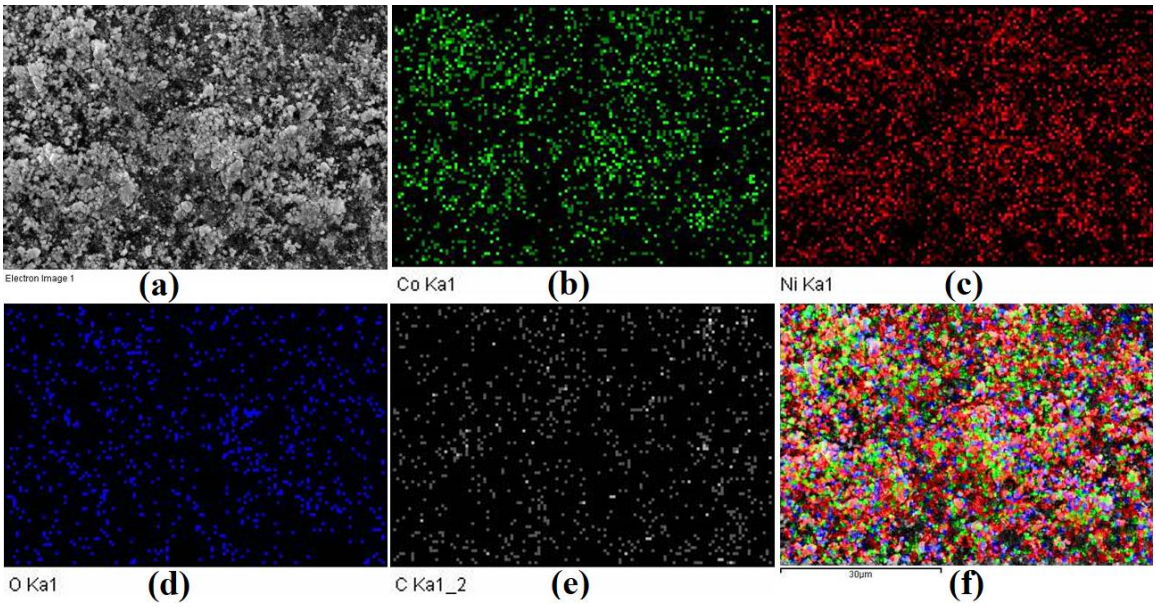

Figure 3.8: Elemental Mapping of CNOG: (a) SEM image, (b)-(e) Mapping images of Co, Ni, O, and C respectively, (f) Superimposed image of Co, Ni, O and C

3.3.2 Physical characterizations

3.3.2.1 X-ray Diffraction (XRD)

The XRD patterns of NCO, CNO and CNOG are displayed in fig. 3.9a. In the XRD pattern of NCO, characteristic diffraction peaks appear at 18.9˚, 31.41˚, 36.8˚, 44.7˚, 59˚, 65.3˚ and 77.2˚ corresponding to (111), (220), (311), (400), (511), (440), and (533) planes respectively of the $NiCo_2O_4$ spinel structure (JCPDS No- 73-1702)) [31]. The diffraction peaks corroborate well with the standard pattern of $NiCo_2O_4$ with inverse spinel structure. In CNO, apart from the $NiCo_2O_4$ peaks, additional diffraction peaks are seen at 37.15º, 43.53˚, 62.6˚, 75.2˚, and 79˚. These peaks correspond to NiO planes (111), (200), (220), (311), and (222) respectively (JCPDS No- 73–1519) [32]. The crystal structure formation of CNO can be confirmed as all the planes corresponding to $NiCo_2O_4$ and NiO are observed. Graphene oxide formation is ensured from the diffraction peak (as shown in fig. 3.9b) observed at around 10.3° which corresponds to (002) plane. On reduction of GO, this peak decreases in intensity and a hump is observed at around 25º, thus confirming the formation of rGO [27, 33] (fig. 3.9a of CNOG). The shift to higher 2θ value results from the partial removal of oxygen-containing functional groups incorporated between the graphene nanosheets caused by the reduction of GO.

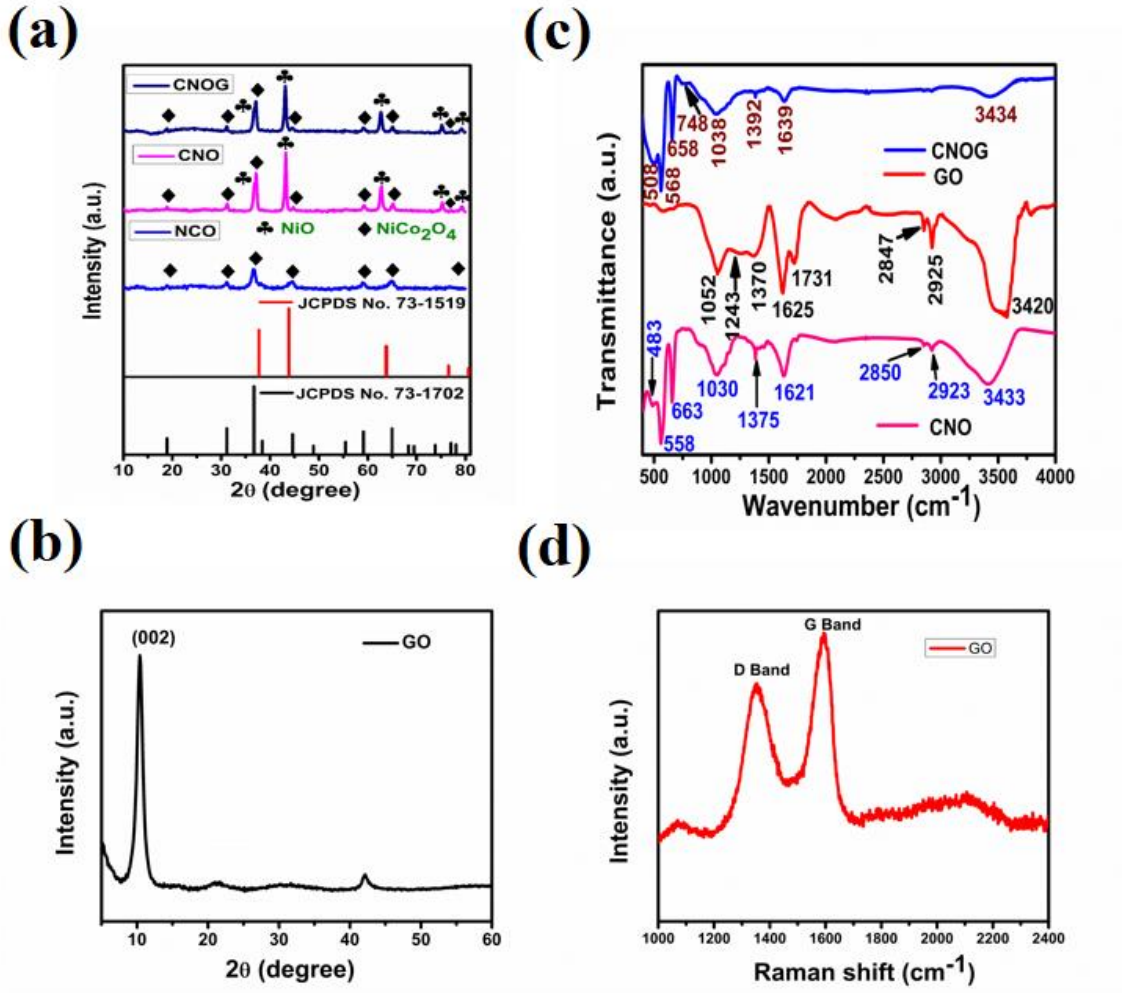

Figure 3.9: Structural characterizations: (a) XRD pattern of NCO, CNO and CNOG, (b) XRD of GO, (c) FTIR spectra of CNO, GO and CNOG, (d) Raman spectrum of GO

3.3.2.2 Fourier transform infrared spectroscopy (FTIR) and Raman Spectroscopy

FTIR spectrum of CNO (shown in fig. 3.9c) consists of vibrational bands at 483, 558, 663, 1030, 1375, 1621, 2850, 2923, 3433 cm^{-1} which correspond to Ni-O antisymmetric stretching vibrations of NiO, Co-O stretching vibration, Ni-O stretching vibration of $NiCo_2O_4$, bending vibration of H_2O molecule, C-O bond, bending mode of H_2O molecule, symmetric and asymmetric CH_2 stretching, O-H stretching mode of water molecule respectively [34, 16, 35]. The FTIR spectrum of GO in fig. 3.9c confirms the presence of its functional groups. Vibrational bands are observed at 1052, 1243, 1370, 1625, and 1731 cm^{-1}, which correspond to C-O alkoxy, C-O epoxy, C-O carboxyl, C=C, and C=O stretching of carboxyl group, respectively. Additional bands appear at 2847,

2925, and 3420 cm^{-1}, which appear due to symmetric CH_2 stretching, asymmetric CH_2 stretching, and O-H stretching of H_2O molecules. In the nanocomposite CNOG, all the vibrational bands of CNO are found in addition to C=C band of graphene. A weak absorption peak appears at 748 cm^{-1}, which corresponds to metal-oxygen vibrations [34]. When GO is converted to rGO, all of the vibrational bands corresponding to the epoxy and carboxyl groups vanish. Moreover, the Raman spectrum of GO prove the successful formation of GO. In the Raman spectrum of GO shown in fig. 3.9d, the D and G bands are observed at 1330 and 1583 cm^{-1} respectively. The D band represents the breathing modes of carbon with A_{1g} symmetry, which represent the presence of defects in GO, and G band corresponds to first order scattering from E_{2g} phonon modes of sp^2 hybridized C atoms in GO [33].

3.3.2.3 X-ray photoelectron spectroscopy (XPS)

XPS was performed to understand the chemical bonds and redox states of the metal ions Ni and Co in CNO and CNOG nanocomposite. The full-scan survey in fig. 3.10a confirms the presence of elements Ni, Co, O, and C in CNO and CNOG. The C 1s peak of CNO arises because of the residual HMT used in the synthesis of CNO; whereas in CNOG, the C 1s peak occurs due to rGO nanosheets and residual HMT. To better visualize the multiple deconvoluted spectra, differential graphs of intensity versus binding energy of each deconvoluted spectrum are plotted and displayed in fig. A1 in Appendix A)**.** As seen in fig. 3.10b, Ni 2p of CNO exhibits two peaks at 854.11 and 871.57 eV attributed to Ni^{2+} of $2p_{3/2}$ and $2p_{1/2}$ spin-orbit doublets respectively. The presence of Ni^{3+} state is established by the peaks appearing at 855.79 and 873.29 eV arising due to Ni^{3+} $2p_{3/2}$ and $2p_{1/2}$, respectively [29, 36]. The two satellite peaks around 861.23 and 879.26 eV further confirm the existence of both Ni^{2+}/Ni^{3+} oxidation states. Another peak appears at 865 eV in both CNO and CNOG; this peak refers to satellite peak of Ni $2p_{3/2}$ in NiO [37, 38]. On adding reduced graphene oxide to CNO, the peaks evolve at slightly higher value of binding energy (i.e., at 854.15, 855.86, 861.25, 871.65, 873.41, 879.35 eV) suggesting that the electron transfer is taking place from Ni to its neighbouring rGO nanosheets in CNOG. The high-resolution spectra of Co 2p (fig. 3.10c) displays two broad peaks at 780 and 795 eV, which correspond to the spin-orbit doublets $2p_{3/2}$ and $2p_{1/2}$ respectively [37]. On deconvoluting these peaks for CNO, two peaks at 781.16 and 796.6 eV arise due to Co^{2+} state, whereas 779.7, 794.9 eV peaks

correspond to Co^{3+} oxidation state [37]. While in case of CNOG, peaks are observed at 781, 796.48 eV and 779.73, 794.9 eV corresponding to Co^{2+} and Co^{3+} respectively. It is observed that the binding energy of Co^{2+} in CNOG shifts to lower value, which is due to electron transfer from the surrounding to the Co^{2+} ions [38].

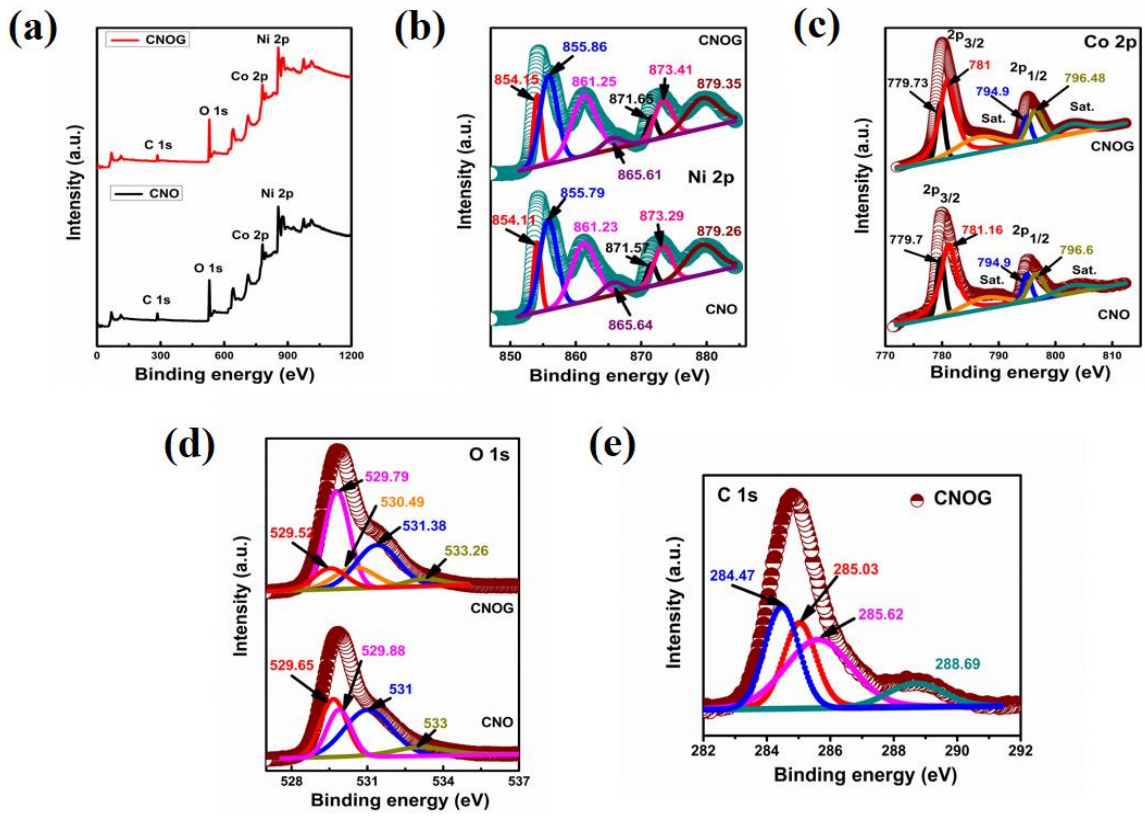

Figure 3.10: XPS of CNO and CNOG: (a) Survey spectra, High-resolution XPS spectra of (b) Ni 2p, (c) Co 2p, (d) O 1s, and (e) C 1s

Two satellite peaks are also observed which confirms the presence of Co^{2+} and Co^{3+} state. O 1s spectra of CNO (shown in fig. 3.10d) are observed at 529.65, 529.88, 531, 533 eV, which correspond to Ni-O bond, Co-O bond, C=O, and O-H bond of physically/chemically adsorbed water molecules, respectively. In case of CNOG, these peaks shift to 529.52, 529.79, 530.49, 531.38, and 533.26 eV [10]. The peaks at 530.49, 531.38 eV correspond to the oxygenated species of the functional group O-C=O and C=O of GO [39]. The increase in binding energy of the peak corresponding to 531 and 533 eV in CNOG is because of the oxidization of the graphene layers. In the C 1s spectra of CNOG (depicted in fig. 3.10e), four peaks appear after deconvolution. The peaks at 284.47, 285.03 eV are ascribed to the C-C and C=C of the graphitic sp^3 and sp^2 hybridised

carbons, respectively [40, 41, 42]. Another two peaks at 285.62 and 288.69 eV correspond to the functional group C-OH (hydroxyl group) and C=O (carboxyl group), respectively [40] due to the addition of reduced graphene oxide nanosheets to CNO.

3.3.2.4 Nitrogen (N_2) adsorption-desorption analysis

The surface area and porosity of the developed materials have been analyzed using BET method. All the catalysts developed are mesoporous in nature and exhibit type IV isotherm (shown in fig. 3.11). Compared to the pristine metal oxides NCO (26 m^2/g) and CNO (47 m^2/g), the hybrid catalyst CNOG exhibit the highest surface area of 53 m^2/g. As obtained from pore size distribution the size of pore lies in the mesopore range 3-7 nm.

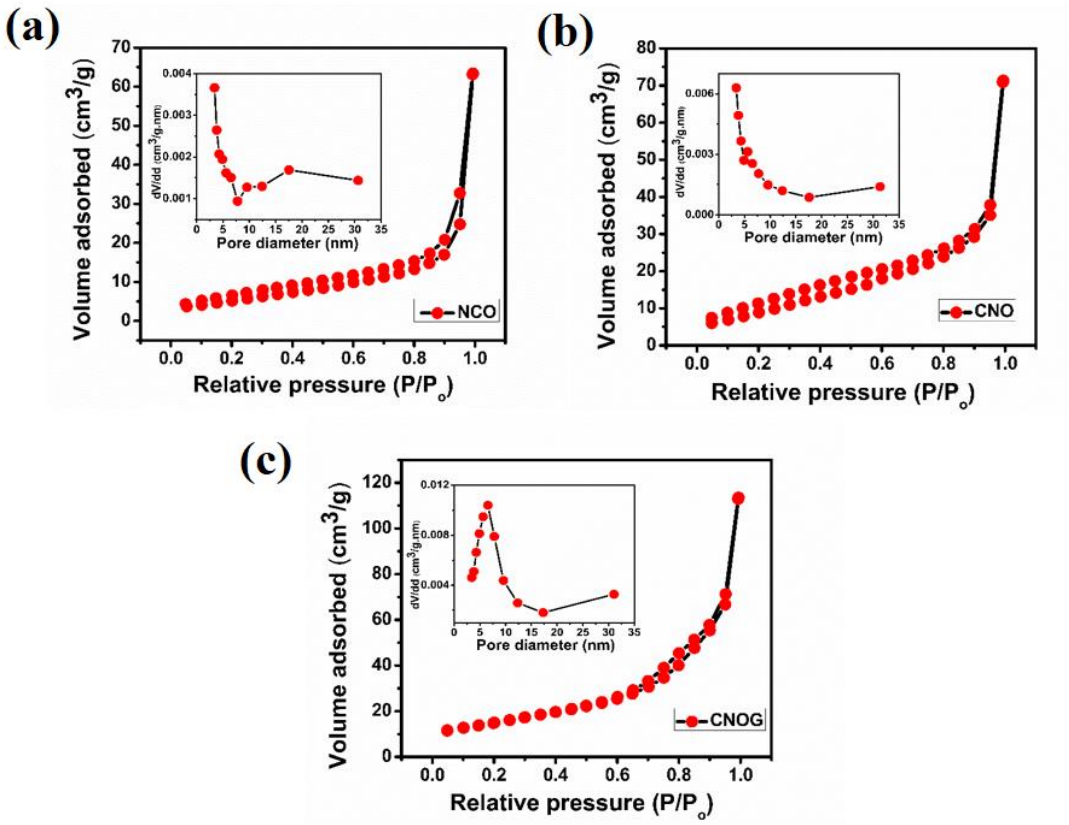

Figure 3.11: N_2 adsorption-desorption isotherms along with pore size distribution in inset (i) NCO, (ii) CNO, (iii) CNOG

3.3.3 Electrochemical characterizations

3.3.3.1 Electrochemical activity of the electrodes in absence of methanol

The electrochemical behaviours of the electrodes (on GCE substrate) are assessed by cyclic voltammetry and as shown in fig. 3.12a, the hybrid electrode CNOG offers the highest current density because of the synergistic contribution of rGO, $NiCo_2O_4$ and NiO. A redox pair is observed which is attributed to the redox couples Co^{2+}/Co^{3+} and Ni^{2+}/Ni^{3+}. The redox reaction governing this peak is- $NiCo_2O_4 + OH^- + H_2O \rightarrow 2CoOOH + NiOOH + e^-$.

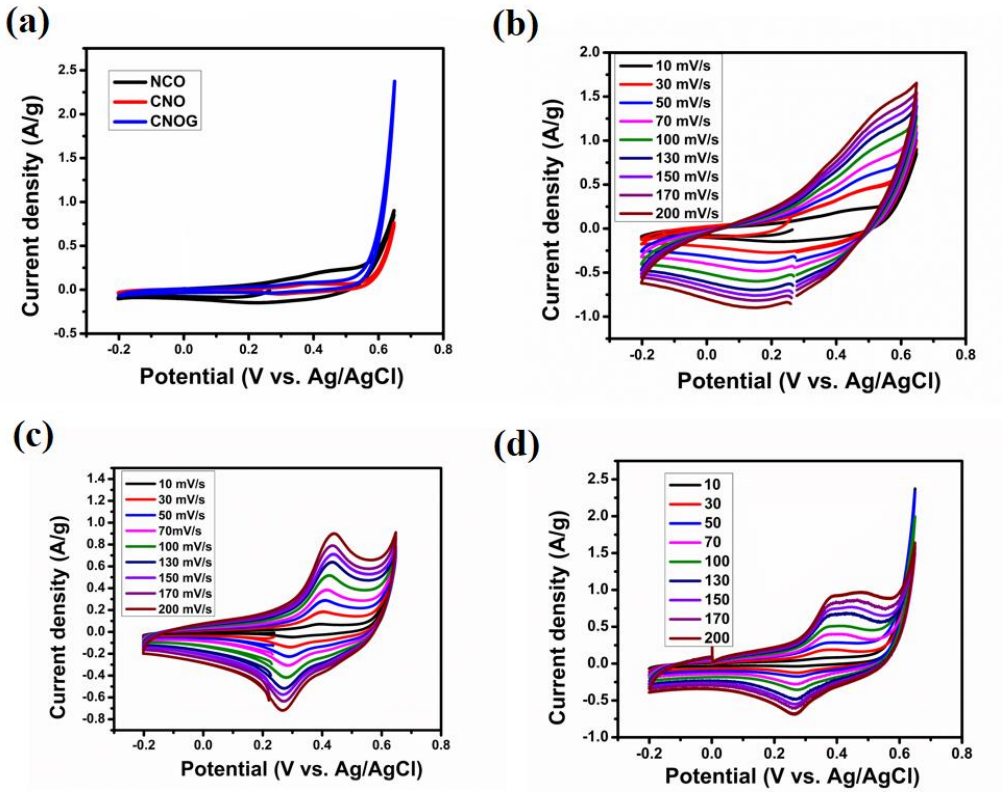

Figure 3.12: Cyclic voltammetry of the electrodes in 0.5 M NaOH - (a) NCO/GC, CNO/GC and CNOG/GC at a 10 mVs^{-1}, (b) NCO/GC, (c) CNO/GC, (d) CNOG/GC at varying scan rate

As scan rate affects the redox reactions, the variation of current density with scan rate is studied for all the three electrodes as shown in fig. 3.12b, c and d. It is seen that with increase in scan rate the peak-to-peak separation, ΔE_p increases; however, the shape of CV remains the same, which represents quasi-reversibility of the electrodes. $NiCo_2O_4$ exhibits the highest ΔE_p value of 237 mV at 10 mV/s scan rate, which decreases by developing the mixed metal oxide composite $NiCo_2O_4$/NiO (ΔE_p = 87 mV). On

developing composite of $NiCo_2O_4$/NiO with rGO nanosheets, the value decreases further to 83 mV in CNOG. The hybrid CNOG offers high surface area and conductivity to the system as a result of which reversibility increases.

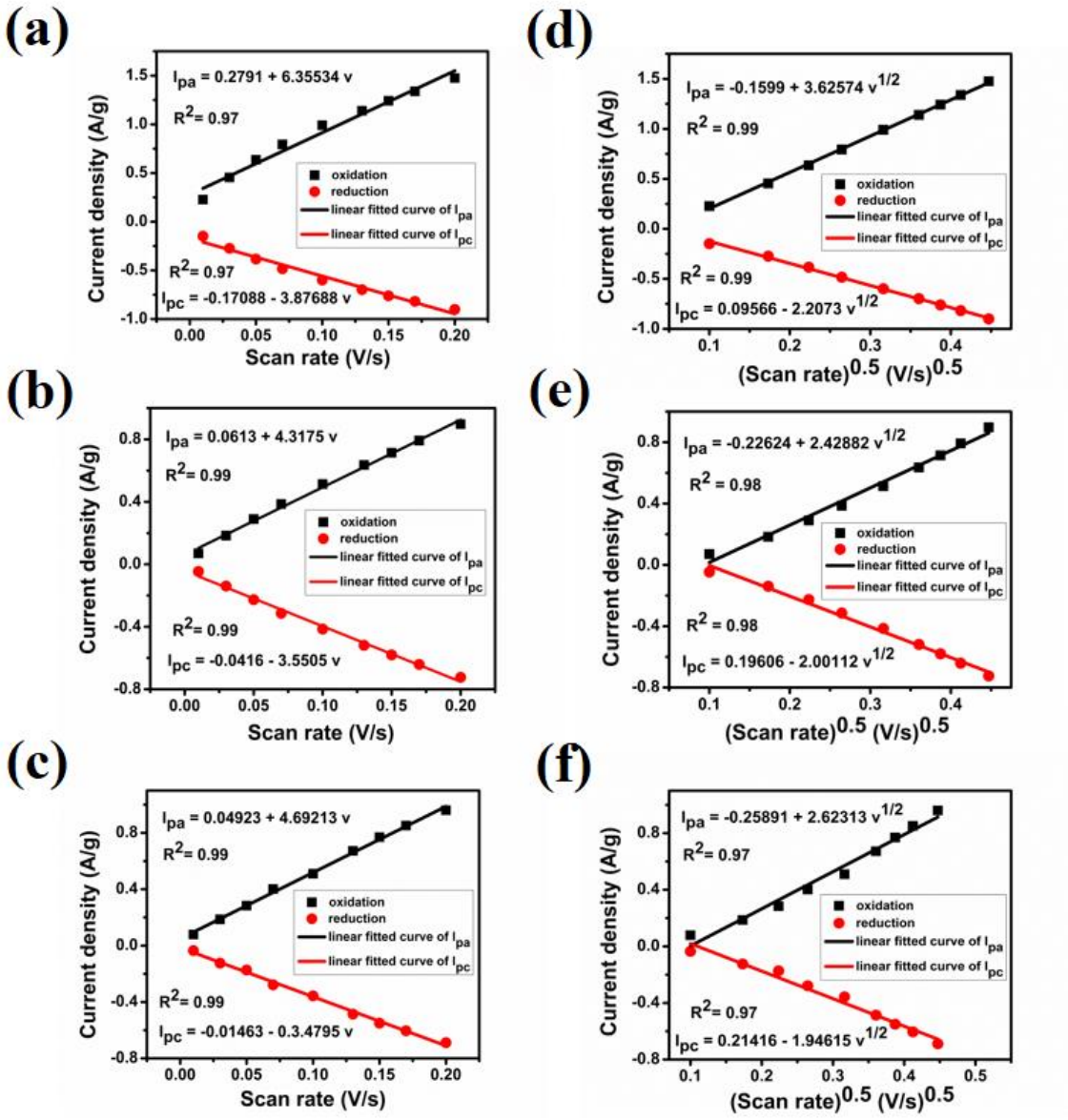

Figure 3.13: (a), (b), (c): I_p vs. ν plot of NCO/GC, CNO/GC, and CNOG/GC respectively. (d), (e), (f): I_p vs. $\nu^{1/2}$ plot of NCO/GC, CNO/GC, and CNOG/GC respectively

Furthermore, it is clear from fig. 3.13 that all the three electrodes exhibit the surface adsorbed process and the diffusion-controlled process, since the peak current density (I_p) varies linearly with both scan rate, ν (fig. 3.13a, b, c), and square root of scan rate (fig.

3.13d, e, f), respectively. It is also evident from the slope of log I_p vs log ν plot (fig. 3.14a) which is equal to 0.6, 0.8 and 0.8 for NCO, CNO, and CNOG respectively. The surface coverage of adsorbed redox species is calculated to be 3.4×10^{-5}, 2.3×10^{-5}, and 2.5×10^{-5} mol/g.cm^2, respectively for NCO, CNO, and CNOG, based on Brown-Anson model [43]. Using Laviron's method (Laviron's plot displayed in fig. 3.14b, c, d), the electron transfer coefficient (α) and heterogeneous rate constant (k_s) are calculated and listed in table 3.1. The enhanced value of α and k_s of CNOG indicate that the interfacial contact between the metal oxides and graphene increases the kinetics of the redox reactions by providing more channels for ions to access the active sites. Additionally, the mesopores and large surface area of CNOG facilitate increased electron transfer by reducing the diffusion path of ions.

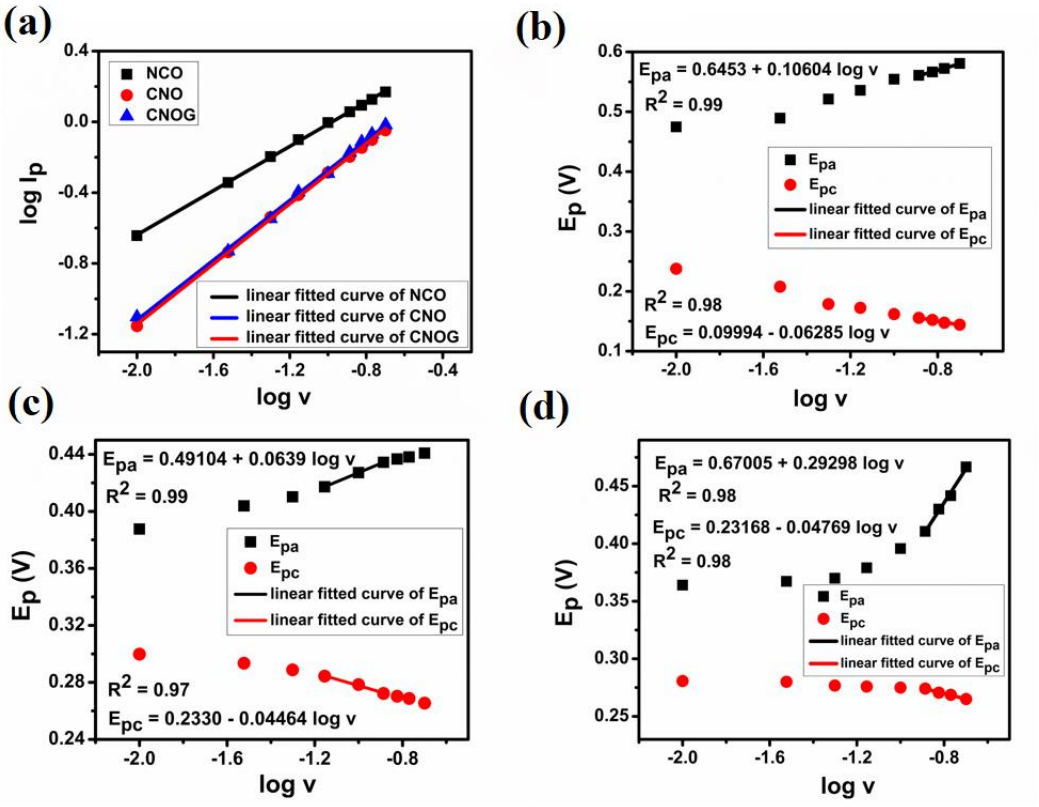

Figure 3.14: (a) Plot of logarithm of peak anode current density vs. logarithm of scan rate, Laviron's plot: (b) NCO/GC, (c) CNO/GC, (d) CNOG/GC

Table 3.1: α and k_s value of the electrodes

Catalyst	Anodic electron transfer coefficient (α)	Average heterogeneous rate constant (k_s)
$NiCo_2O_4$	0.4	0.05
$NiCo_2O_4$/NiO	0.07	0.22
$NiCo_2O_4$/NiO/rGO	0.79	0.56

3.3.3.2 Electrochemical activity of the electrodes in presence of methanol

Cyclic voltammetry is used to investigate the catalysis of the methanol oxidation process (MOR) at methanol concentrations ranging from 1 to 6 molar. Figure 3.15a shows the CV of all the electrodes in 3 M methanol at 50 mV/s sweep rate. Among the three, CNOG exhibits the highest current density. Figures 3.15b, c, and d show the cyclic voltammograms of NCO, CNO, and CNOG at a scan rate of 200 mV/s. In all the three electrodes, 3 M is obtained as the optimized methanol concentration. MOR current beyond 3 M concentration decreases due to reaction-kinetics controlled process [44]. CNOG/GC offers the highest current density of 26.86 A/g at 200 mV/s. The onset potential obtained for CNOG/GC, CNO/GC and NCO/GC catalysts are 0.32, 0.36, 0.40 V respectively at 50 mV/s. rGO nanosheets, $NiCo_2O_4$ nanoflakes, and NiO nanoparticles render CNOG large specific surface area and more exposed active sites. The poor conductivity and tendency of metal oxide nanostructures to agglomerate or dissolve during the methanol oxidation reduces their catalytic activity. When these transition metal oxide nanostructures $NiCo_2O_4$/NiO are grown on rGO nanosheets, the resulting hybrid structure increases the conductivity and structural stability of the catalyst CNOG. Co^{2+} and Ni^{2+} get oxidised to higher oxidation state Co^{3+} and Ni^{3+}, which get reduced back to the lower state (II) after accepting an electron from methanol molecule. Thus, NiOOH and CoOOH are the reactive oxidising species present on the catalysts. So, the probable chemical reactions involved in methanol oxidation reaction can be expressed by equations 3.1-3.2.

$$NiOOH + CH_3OH + 1.25O_2 \rightarrow Ni(OH)_2 + CO_2 + 1.5H_2O \quad (3.1)$$

$$2CoOOH + 2CH_3OH + 2.5O_2 \rightarrow 2Co(OH)_2 + 2CO_2 + 3H_2O \quad (3.2)$$

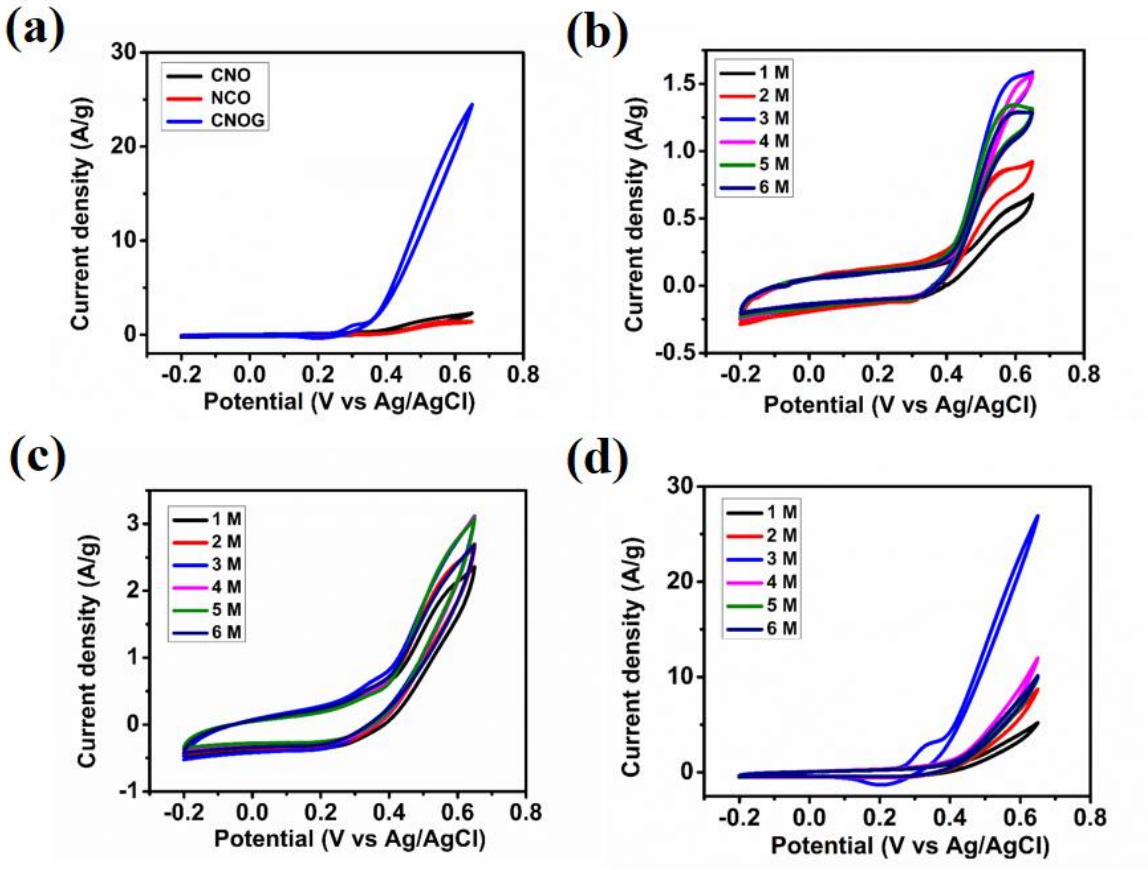

Figure 3.15: Cyclic voltammetry in presence of methanol: (a) NCO/GC, CNO/GC, and CNOG/GC at 50 mVs^{-1} in 0.5 molar sodium hydroxide solution in 3 molar CH_3OH, (b) NCO/GC, (c) CNO/GC, (d) CNOG/GC at varying concentrations of CH_3OH at 200 mV/s

To see the effect of scan rate on MOR, the scan rate is varied from 10-200 mV/s and the scan rate varied CV profiles are displayed in fig. 3.16a-3.16c, where MOR current increases with scan rate. With increase in scan rate, the cathodic current density of Co(III)/Co(II) and Ni(III)/Ni(II) conversions increases, which suggests the availability of more active sites for MOR. Thus, the MOR current increases at higher scan rate, which occurs due to the high conductivity and porosity of the electrodes. The kinetics of MOR is studied using Tafel equation [45] given by $E_p = \frac{2.303RT}{\alpha nF}[logI_p - logI_o]$, where, E_p represents overpotential, I_p and I_o denotes methanol oxidation current and exchange current density respectively, α being the electron transfer coefficient, and F is the Faraday constant.

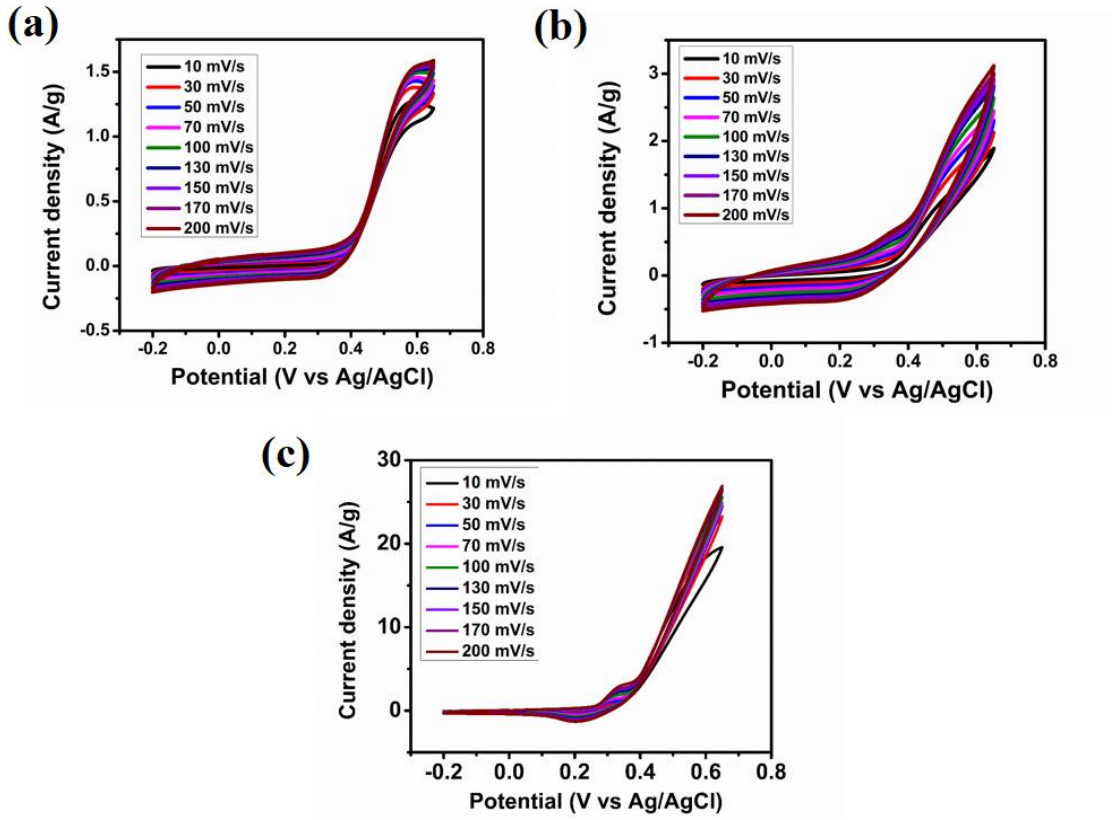

Figure 3.16: Cyclic voltammetry in presence of methanol: (a) NCO/GC, (b) CNO/GC, and (c) CNOG/GC in 3 molar CH_3OH at varying scan rate

A smaller Tafel slope (slope of $E_p\ vs.\ logI_p$ plot) characterizes a good electrocatalyst. Electron transfer coefficient and Tafel slope of all the electrodes are listed in table 3.2. Figure 3.17a represents Tafel plot of NCO, and fig. 3.17b and c corresponds to that of CNO at low and high potential respectively. As displayed in fig. 3.17b and c, the Tafel plot of CNO exhibits two slopes which suggests the presence of two different rate determining step dependent on the operating potentials [46]. Similarly, CNOG exhibits two slopes depending on the potential (shown in fig. 3.17d and e). At potential up to 0.46 V vs. Ag/AgCl, Tafel slope of 77 mV/dec is obtained; and beyond that, higher Tafel slope of 317 mV/dec is attained. Low Tafel slope favours methanol oxidation, whereas higher slope is the indicator of catalyst degradation by CO intermediates. Minimum Tafel slope and highest electron transfer coefficient of CNOG suggest better kinetics of methanol oxidation. The potential dependent Tafel slope of the electrodes manifest adsorption of

the oxidation intermediate products on the catalyst surfaces and oxidation of these products interferes methanol oxidation [47].

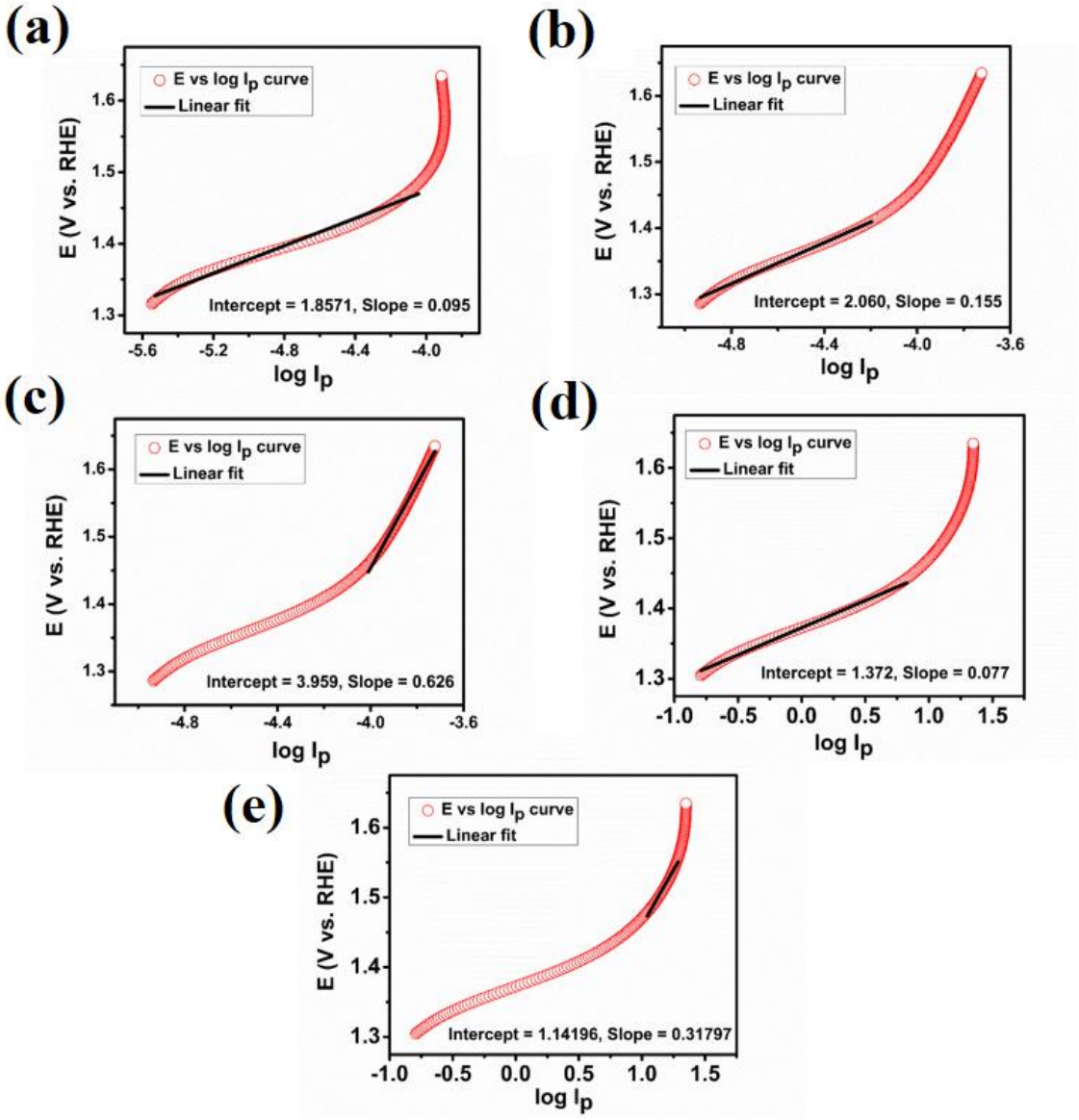

Figure 3.17: Tafel plot in 3 M methanol at 10 mVs^{-1}: (a) NCO/GC, (b) CNO/GC at low overpotential, (b) CNO/GC at high overpotential, (d) CNOG/GC at low over potential, (e) CNOG/GC at high over potential

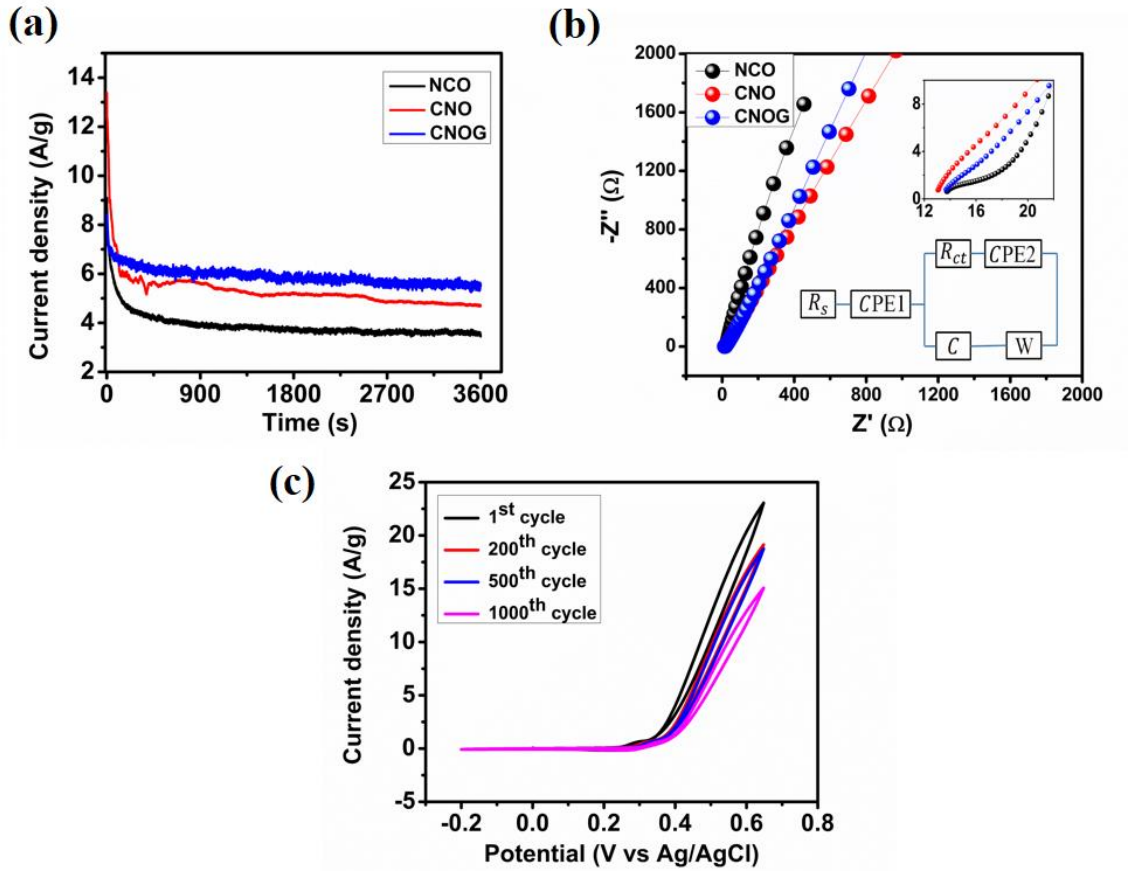

Figure 3.18: (a) Chronoamperograms of NCO/GC, CNO/GC, and CNOG/GC in 3 molar CH_3OH at 0.65 V for 1 hr, (b) Nyquist plots (Top inset: zoomed view of higher frequency Nyquist plot, bottom inset: equivalent circuit), (c) Cycling stability of CNOG/GC at a 30 mVs^{-1} in 3 molar CH_3OH

Electrochemical stabilities of the electrodes are assessed by chronoamperometry for 1 hr and are displayed in fig. 3.18a. The current decreases for the first 400 s due to coverage of the catalyst surface by CO and oxidation intermediate products, and remains constant thereafter. The tolerance to these CO intermediates can be measured quantitatively by a parameter called deterioration rate. Lower deterioration rate implies better tolerance. The deterioration rate and retention of current of the three catalysts are tabulated in table 3.2. CNOG offers the lowest deterioration rate and highest current retention, which suggest better durability of the catalyst. The hydroxyl groups present on the surface of rGO nanosheets react with the adsorbed CO to form CO_2, thereby releasing the active sites free from CO. To understand the reaction kinetics and processes EIS was performed in 3

M methanol solution containing 0.5 M NaOH as the supporting electrolyte (shown in fig. 3.18b). In order to get proper understanding, the experimental data are fitted with electrochemical circuit model (shown in inset of fig. 3.18b) consisting of series resistance (R_s), charge transfer resistance (R_{ct}), constant phase element (CPE), capacitance (C), and Warburg impedance (W). In the high frequency region, the semicircle represents the presence of RC circuit. The high and intermediate frequency region is dominated by charge transfer kinetics, whereas the low frequency region is dominated by mass transfer i.e. diffusion of ions [48]. The intercept of the X-axis gives the R_s and the diameter of the first semicircle give the R_{ct} value. Amongst all the three electrodes, CNOG offers the least charge transfer resistance (6 Ω); whereas NCO and CNO shows 7.8 Ω and 11.65 Ω respectively. On making the binary composite of $NiCo_2O_4$ with NiO, the charge transfer resistance of CNO becomes higher than NCO, which may be due to the presence of more oxides in the system, which is again compensated by CNOG due to the presence of conducting rGO nanosheets. The constant phase element used in the circuit represents the heterogeneous properties of the active material arising due to mesopores of the electrodes. In the lower frequency region, lower value of Warburg diffusion coefficient corresponds to easy access of electrolyte ions into the electrode's active sites. The slope of the Nyquist plot of CNOG is almost 45º at low frequency, which suggests good ionic diffusion. Thus, better conductivity, high surface area, presence of pores, multiple redox sites exposed to the surface, and the layer-on-layer structure of CNOG provide excellent electrode-electrolyte interaction and favours methanol oxidation reaction. Durability of the catalyst CNOG is studied by observing CV for 1000 cycles at 3 M methanol and 30 mV/s scan rate as shown in fig. 3.18c. It is observed that MOR current does not decrease much with current retention of 83.34%, 81.47% and 65.63% after 200^{th}, 500^{th} and 1000^{th} cycles respectively. The 65.63% current retention even after 1000^{th} cycle corroborates well with the low deterioration rate obtained from chronoamperometry study. The minimal current decay is mainly due to the blocking of the active sites of the catalyst by the oxidation intermediates byproducts.

Table 3.2: Tafel slope, Electron transfer coefficient, Calculated values of current retention and Deterioration rate of all the electrodes

Sl. No.	Catalyst	Tafel slope (mV/dec)	Electron Transfer Coefficient α (s^{-1})	Retention %	Deterioration rate (s^{-1})
1	NCO	95	0.62	38	5.7×10^{-5}
2	CNO	155 (V < 0.46 V vs. Ag/AgCl) 626 (V > 0.46)	0.38 (V < 0.46) 0.09 (V > 0.46)	35	4.7×10^{-5}
3	CNOG	77 (V < 0.46 V vs. Ag/AgCl) 317 (V > 0.46)	0.76 (V < 0.46) 0.18 (V > 0.46)	66	4×10^{-5}

3.3.4 Characterizations of the electrode after cycling stability

After the stability test, XPS was done to know the changes in chemical states of the catalyst after the methanol oxidation process. It is seen that after active participation in methanol oxidation, the intensity of Ni 2p and Co 2p orbitals (fig. 3.19a) decreases; which suggests the degradation of catalyst over time. As observed from fig. 3.19b, the binding energy increment of Ni^{2+} $2p_{3/2}$, Ni^{3+} $2p_{3/2}$ and Ni^{3+} $2p_{1/2}$ implies the charge transfer taking place on Ni sites. The disappearance of 865 eV satellite peak after methanol oxidation occurs due to charge transition from O 2p to Ni 3d states of NiO [38]. The binding energy of Ni^{2+} $2p_{1/2}$ decreases which may be due to accumulation of electron density near these sites produced during oxidation of methanol molecules. Moreover, the decrease in intensity of all the Ni peaks signifies the decrease in Ni content after the methanol oxidation. The loss of Ni content may be due to degradation of the catalyst surface and dissolution of Ni ions. As depicted in fig. 3.19c, Co 2p spectra upon deconvolution shows similar trend in binding energy enhancement, which confirms the redox reactions taking place on these Co sites as well. One additional peak centred at 773.26 eV appears whose origin is still not understood.

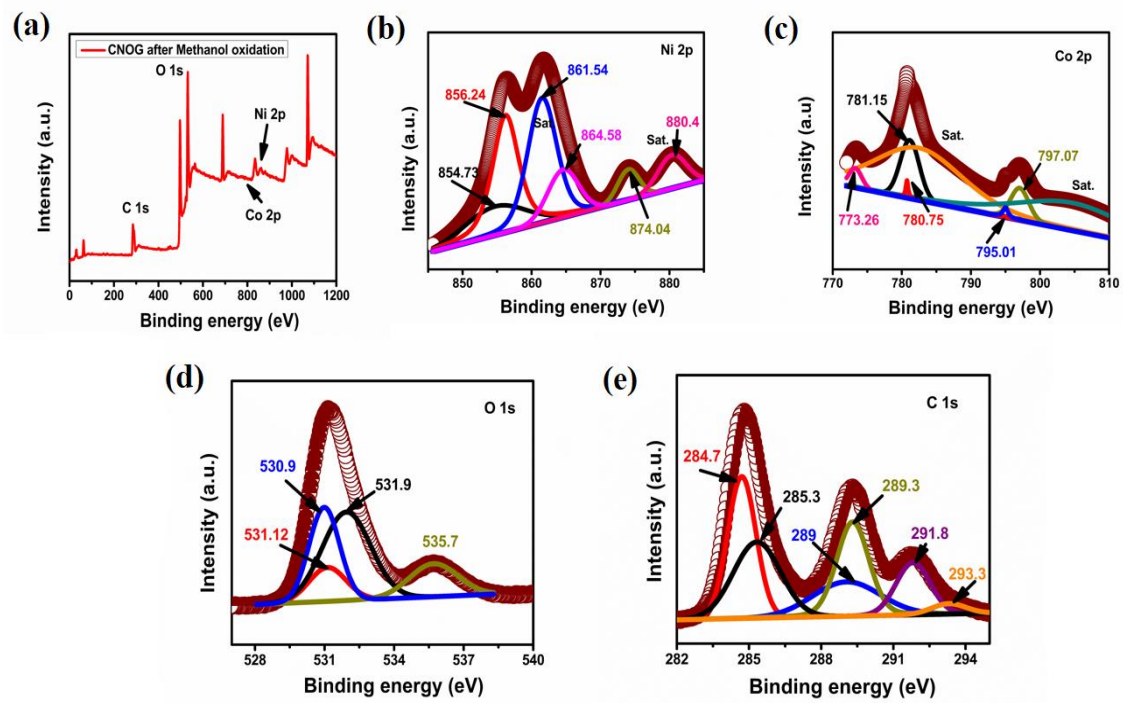

Figure 3.19: XPS of CNOG after methanol oxidation: (a) Survey spectra, High-resolution XPS spectra of (b) Ni 2p, (c) Co 2p, (d) O 1s, and (e) C 1s

In the O 1s spectra (fig. 3.19d), the Co-O peak appears at 530.9 eV, whereas the Ni-O peak disappears due to decrease in Ni content due to degradation of the catalyst. The other two interactions (O-C=O and C=O) also change their binding energy to higher value due to oxidation taking place. An additional peak appears in O 1s spectra at 535.7 eV which is attributed to formaldehyde formed as an oxidation by-product of methanol. After the methanol oxidation is processed for a longer time period, the C 1s exhibits 6 peaks at 284.7, 285.3, 289, 289.3, 291.8, and 293.3 eV. The 284.7, 285.3, 289, and 289.3 peaks correspond to C-C, C=C of sp^2 hybridized carbon atoms and C-OH (hydroxyl), and C=O (carboxyl) groups, respectively of rGO nanosheets (fig. 3.19e). The extra peaks 291.8 and 293 eV correspond to CHO compound mainly formaldehyde [49, 50], and formate [51] formed as a product of methanol oxidation. It is observed that post methanol oxidation, the 285.3 peak increases in area, which is due to overlapping of C=C interaction with methoxy, formed as a by-product [52].

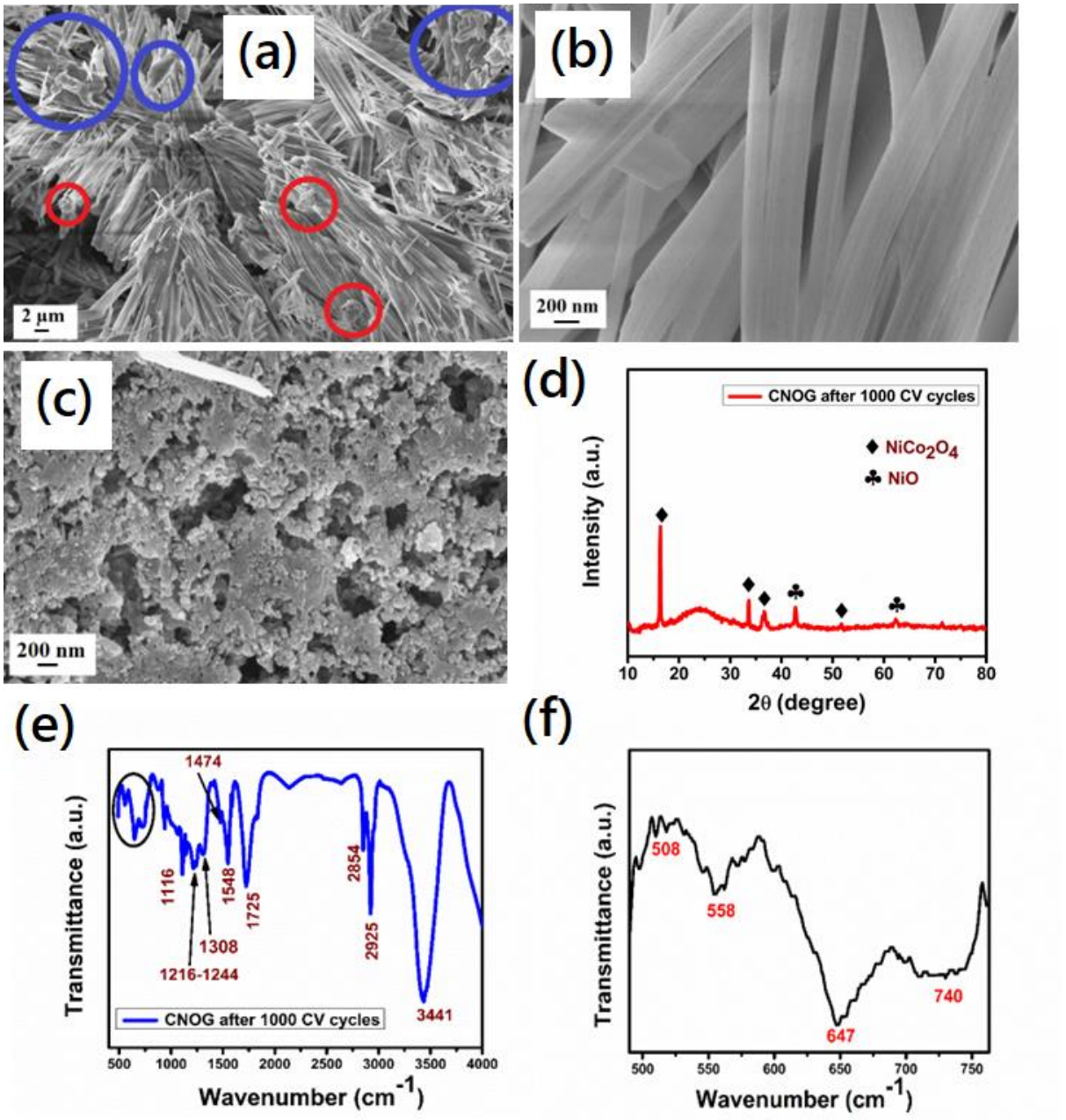

Figure 3.20: Characterizations of CNOG after methanol oxidation: (a)–(c) FESEM images. In fig. 3.20a, the red circles are displaying the lumps and blue circles marking the fragmentation of $NiCo_2O_4$ flakes, (d) XRD, and (e)-(f) FTIR pattern after 1000 CV cycles in 3 molar CH_3OH + 0.5 molar sodium hydroxide aqueous solution

The hybrid CNOG appears fibre-like structure after oxidation of methanol for 1000 CV cycles (as shown in fig. 3.20a, b). The enlarged view of the fig. 3.20a are displayed separately in fig. 3.21a and 3.21b to see clearly the agglomeration lumps and restacking,

respectively. Morphology change in CNOG after continuous methanol oxidation is mainly due to the catalytic reactions taking place on its surface leading to dissolution and redistribution of the metal oxides $NiCo_2O_4$, NiO and rolling of rGO nanosheets [53, 54]. The areas marked by red circles in fig. 3.20a and 3.21a display lumps of $NiCo_2O_4$ and NiO scattered on the nanofiber matrix of rGO.

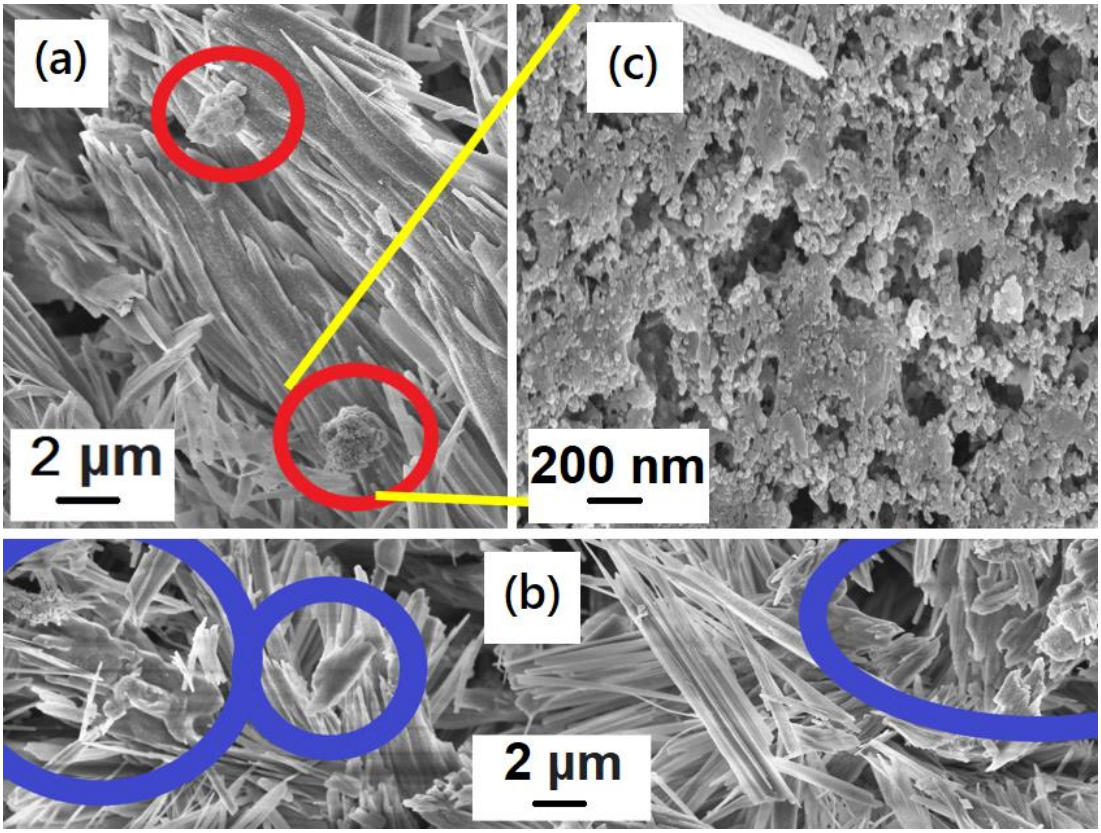

Figure 3.21: FESEM of CNOG after methanol oxidation: (a) Enlarged image of fig. 3.20a. Red circles are marking the lumps, (b) Enlarged image of fig. 3.20a. The areas marked by blue circles are displaying the non-uniform restacking and fragmentation of $NiCo_2O_4$ flakes, (c) Magnified image of the lumps shown inside red circle in fig. 3.21a.

The magnified image of the lump can be seen in fig. 3.20c and 3.21c, where the agglomeration can be observed. The restacking and fragmentation of the $NiCo_2O_4$ flakes can be observed in the areas marked by blue circles in fig. 3.20a and 3.21b. Thus, the NiO nanoparticles agglomerate and $NiCo_2O_4$ flakes do not retain their regular stacking pattern. As the dimension of the $NiCo_2O_4$ and NiO are smaller than the nanofiber dimension, so the agglomeration of $NiCo_2O_4$ and NiO are seen only in few places as they may be covered by the rGO nanofibers. However, the agglomeration and restacking can

be seen in few places as confirmed from the portions shown inside the red and blue circles, respectively in the FESEM image. The resulting morphology decreases the interfacial interactions and inhibits the electrolyte ions from reaching the active sites, thereby reducing methanol oxidation.

To observe any new structural phase and to monitor the structural stability of the catalyst after methanol oxidation, XRD was performed. As observed in fig. 3.20d, the XRD peak corresponding to (111) plane of $NiCo_2O_4$ shifts to lower value (16.36°) which may be due to insertion of methanol and other electrolyte ions inside the $NiCo_2O_4$ nanosheets, which leads to increase in interplanar distance. The other XRD peaks decrease in intensity which implies the reduction in crystallinity of the sample. The change in vibrational absorption bands of the catalyst after methanol oxidation was monitored by FTIR and are displayed in fig. 3.20e and 3.20f. As shown in fig. 3.20f (the magnified view of the portion shown by circle in fig. 3.20e), in the wavenumber range 450-750 cm^{-1}, the absorption peaks of CNOG shifts to lower wavenumber value which suggests modification of electron distribution of the molecular bonds Ni-O and Co-O. This modification of electronic distribution occurs as a result of increase in bond length due to changing electronegativity of the neighbouring atoms. Moreover, the decreased intensity of these absorption peaks implies the utilization of these molecules in methanol oxidation reaction. The vibrational bands in the wavenumber region 1116-1308 cm^{-1} occur due to bending of water molecules. A weak peak appears at 1474 cm^{-1} which arises because of adsorbed methanol molecules. As shown in fig. 3.20e, the increased intensity of 2852, 2925, and 3441 cm^{-1} infers the fact that after prolonged methanol oxidation, the catalyst surface gets covered with methoxy species, methanol molecules, and water molecules, respectively [10], which corroborates well with the XPS results. Two additional absorption peaks appear at 1548 and 1725 cm^{-1} which correspond to carboxylic acid functional groups attached to the catalyst surface [55, 56].

3.4 Conclusion

In conclusion, a mesoporous electrode material $NiCo_2O_4$/NiO/rGO (CNOG) is developed as anode catalyst for methanol oxidation. FESEM and TEM images clearly reveal the layer-on-layer morphology of the nanocomposite CNOG. Low conductivity and aggregation issues of transition metal oxides are compensated by making nanocomposite of $NiCo_2O_4$/NiO with conducting reduced graphene oxide. The layer-on-layer structure

of hybrid CNOG enlarges the surface area and increases interfacial interactions among the components. The mesopores facilitate rapid ion transfer by reducing the diffusion paths of ions and increasing electrode-electrolyte interactions. CNOG exhibits surface-controlled as well as diffusion-controlled process. Higher electron transfer coefficient and heterogeneous rate constant of the hybrid CNOG lead to more methanol oxidation current, which occurs due to the presence of conducting rGO nanosheets and the strong interfacial interconnections among the individual components. Methanol current density of 26.86 A/g is obtained with low onset potential of 0.32 V vs Ag/AgCl. The hybrid electrode offers less charge transfer resistance due to the conducting network of reduced graphene oxide and the developed good interfacial interactions. Low Tafel slope of 77 mV/dec, low deterioration rate and good MOR current retention (65.63%) after 1000 CV cycles suggest better stability and reactivity of CNOG as anode catalyst. Formaldehyde, formate, methoxy are expected intermediates products of methanol oxidation as confirmed by post methanol oxidation XPS and FTIR results. The decrease in crystallinity and reduction in intensity of vibrational bands are observed due to utilization of the active sites of the catalyst and degradation of the catalyst over time. After continuous methanol oxidation, the morphology of CNOG changes to fibre-like structure which reduces the efficiency of the catalyst after prolonged use. Thus, CNOG proves itself a durable and efficient anode catalyst for methanol oxidation.

3.5 References:

1. Yaqoob, L., Noor, T. and Iqbal, N. Recent progress in development of efficient electrocatalyst for methanol oxidation reaction in direct methanol fuel cell. *Int J Energy Res*., 45 (5):6550-6583, 2021.
2. Baruah, K. and Deb, P. Electrochemically active site-rich nanocomposites of two-dimensional materials as anode catalysts for direct oxidation fuel cells: new age beyond graphene. *Nanoscale Adv*., 3 (13):3681-3707, 2021.
3. Baruah, B. and Kumar, A. PEDOT: PSS/MnO_2/rGO ternary nanocomposite based anode catalyst for enhanced electrocatalytic activity of methanol oxidation for direct methanol fuel cell. *Synthetic Metals*, 245:74-86, 2018.
4. Gong, M., Zhou, W., Tsai, M.C., Zhou, J., Guan, M., Lin, M.C., Zhang, B., Hu, Y., Wang, D.Y., Yang, J. and Pennycook, S.J. Nanoscale nickel oxide/nickel

heterostructures for active hydrogen evolution electrocatalysis. *Nat. Commun.*, 5 (1):4695, 2014.

5. Zhang, G., Xia, B.Y., Wang, X. and Lou, X.W. Strongly coupled $NiCo_2O_4$-rGO hybrid nanosheets as a methanol-tolerant electrocatalyst for the oxygen reduction reaction. *Adv. Mater*., 26 (15):2408-2412, 2014.
6. Rolison, D.R., Hagans, P.L., Swider, K.E. and Long, J.W. Role of hydrous ruthenium oxide in Pt− Ru direct methanol fuel cell anode electrocatalysts: the importance of mixed electron/proton conductivity. *Langmuir*, 15 (3):774-779, 1999.
7. Carraro, F., Vozniuk, O., Calvillo, L., Nodari, L., La Fontaine, C., Cavani, F. and Agnoli, S. In operando XAS investigation of reduction and oxidation processes in cobalt and iron mixed spinels during the chemical loop reforming of ethanol. *J. Mater. Chem. A*, 5 (39):20808-20817, 2017.
8. Liu, J., Choi, H.J. and Meng, L.Y. A review of approaches for the design of high-performance metal/graphene electrocatalysts for fuel cell applications. *J. Ind. Eng. Chem*., 64:1-15, 2018.
9. Wu, J. B., Li, Z. G., Huang, X. H., Lin, Y. Porous Co_3O_4/NiO core/shell nanowire array with enhanced catalytic activity for methanol electro-oxidation. *J. Power Sources*, 224:1-5, 2013.
10. Baruah, K., Deb, P. Enabling methanol oxidation by an interacting hybrid nanosystem of spinel Co_3O_4 nanoparticle decorated MXenes. *Dalton Trans*., 51 (11):4324-4337, 2022.
11. Baruah, B., Biswas, R., Deb, P. Hybrid 2D-1D nanostructure of NiO composited with PEDOT:PSS and rGO: Bifunctional electrocatalyst towards methanol oxidation and oxygen evolution reaction. *Int J Energy Res*., 46 (12):16394-16415, 2022.
12. Cheng, Y.W., Chen, C.H., Yang, S.W., Li, Y.C., Peng, B.L., Chang, C.C., Wang, R.C., Liu, C.P. Freestanding Three-Dimensional CuO/NiO Core–Shell Nanowire Arrays as High-Performance Lithium-Ion Battery Anode. *Sci. Rep*., 8 (1):18034, 2018.
13. Dubal, D.P., Gomez-Romero, P., Sankapal, B.R. and Holze, R. Nickel cobaltite as an emerging material for supercapacitors: an overview. *Nano Energy*, 11:377-399, 2014.
14. Hu, L., Wu, L., Liao, M., Hu, X. and Fang, X. Electrical transport properties of large, individual $NiCo_2O_4$ nanoplates. *Adv. Funct. Mater*., 22 (5):998-1004, 2012.

15. Wang, Y., Zhang, Z., Liu, X., Ding, F., Zou, P., Wang, X., Zhao, Q. and Rao, H. MOF-derived NiO/$NiCo_2O_4$ and NiO/$NiCo_2O_4$-rGO as highly efficient and stable electrocatalysts for oxygen evolution reaction. *ACS Sustainable Chem. Eng*., 6 (9):12511-12521, 2018.
16. Haripriya, M., Sivasubramanian, R., Ashok, A.M., Hussain, S. and Amarendra, G. Hydrothermal synthesis of $NiCo_2O_4$–NiO nanorods for high performance supercapacitors. *J. Mater. Sci.: Mater. Electron*., 30:7497-7506, 2019.
17. Chu, Q., Yang, B., Wang, W., Tong, W., Wang, X., Liu, X. and Chen, J. Fabrication of a Stainless-Steel-Mesh-Supported Hierarchical Fe_2O_3@$NiCo_2O_4$ Core-Shell Tubular Array Anode for Lithium-Ion Battery. *ChemistrySelect*, 1 (17):5569-5573, 2016.
18. Bhagwan, J., Nagaraju, G., Ramulu, B., Sekhar, S.C. and Yu, J.S. Rapid synthesis of hexagonal $NiCo_2O_4$ nanostructures for high-performance asymmetric supercapacitors. *Electrochim. Acta*, 299:509-517, 2019.
19. Jiang, H., Ma, J. and Li, C. Hierarchical porous $NiCo_2O_4$ nanowires for high-rate supercapacitors. *Chem. Commun*., 48 (37):4465-4467, 2012.
20. Wei, C., Zhang, R., Zheng, X., Ru, Q., Chen, Q., Cui, C., Li, G. and Zhang, D. Hierarchical porous $NiCo_2O_4$/CeO_2 hybrid materials for high performance supercapacitors. *Inorg. Chem. Front.*, 5 (12):3126-3134, 2018.
21. Mahala, C. and Basu, M. Nanosheets of $NiCo_2O_4$/NiO as efficient and stable electrocatalyst for oxygen evolution reaction. *ACS omega*, 2 (11):7559-7567, 2017.
22. Xiao, Y., Feng, L., Hu, C., Fateev, V., Liu, C. and Xing, W. $NiCo_2O_4$ 3 dimensional nanosheet as effective and robust catalyst for oxygen evolution reaction. *RSC Advances*, 5 (76):61900-61905, 2015.
23. Wei, C., Sun, J., Zhang, Y., Liu, Y., Guo, Z., Du, W., Liu, L. and Zhang, Y. Hierarchical $Ni(OH)_2$–MnO_2 hollow spheres as an electrode material for high-performance supercapacitors. *Inorg. Chem. Front*., *9* (14):3542-3551, 2022.
24. Wei, C., Chen, Q., Cheng, C., Liu, R., Zhang, Q. and Zhang, L. Mesoporous nickel cobalt manganese sulfide yolk–shell hollow spheres for high-performance electrochemical energy storage. *Inorg. Chem. Front*., 6 (7):1851-1860, 2019.
25. Cheng, H., Su, Y.Z., Kuang, P.Y., Chen, G.F. and Liu, Z.Q. Hierarchical $NiCo_2O_4$ nanosheet-decorated carbon nanotubes towards highly efficient electrocatalyst for water oxidation. *J. Mater. Chem. A*, 3 (38):19314-19321, 2015.

26. Xia, W.Y., Li, N., Li, Q.Y., Ye, K.H. and Xu, C.W. Au-$NiCo_2O_4$ supported on three-dimensional hierarchical porous graphene-like material for highly effective oxygen evolution reaction. *Scientific reports*, 6 (1):23398, 2016.
27. Sarmah, D. and Kumar, A. Symmetric supercapacitors with layer-by-layer molybdenum disulfide-reduced graphene oxide structures and poly (3, 4-ethylenedioxythiophene) nanoparticles nanohybrid electrode. *J. Energy Storage*, 35:102289, 2021.
28. Marcano, D.C., Kosynkin, D.V., Berlin, J.M., Sinitskii, A., Sun, Z., Slesarev, A., Alemany, L.B., Lu, W. and Tour, J.M. Improved synthesis of graphene oxide. *ACS nano*, 4 (8):4806-4814, 2010.
29. Zeng, X., Zhao, C., Yin, Y., Nie, T., Xie, N., Yu, R. and Stucky, G.D. Construction of Sandwich-Like $Ti_3C_2T_x$ Mxene-$NiCo_2O_4$ Heterostructure for Remarkable Electromagnetic Microwave Absorption. Available at SSRN 4004901.
30. Zou, Y. and Wang, Y. NiO nanosheets grown on graphene nanosheets as superior anode materials for Li-ion batteries. *Nanoscale*, 3(6):2615-2620, 2011.
31. Jiang, H., Ma, J. and Li, C. Hierarchical porous $NiCo_2O_4$ nanowires for high-rate supercapacitors. *Chem Commun*., 48 (37):4465-4467, 2012.
32. Wang, H., Gao, Q. and Jiang, L. Facile approach to prepare nickel cobaltite nanowire materials for supercapacitors. *small*, 7 (17):2454-2459.
33. Baruah, B. and Kumar, A. rGO/PEDOT: PSS/$NiMn_2O_4$ nanohybrid: an inexpensive anode catalyst for methanol and ethylene glycol electro-oxidation. *J. Electrochem. Soc*., 168 (3):034510, 2021.
34. Yu, M., Chen, J., Liu, J., Li, S., Ma, Y., Zhang, J. and An, J. Mesoporous $NiCo_2O_4$ nanoneedles grown on 3D graphene-nickel foam for supercapacitor and methanol electro-oxidation. *Electrochim. Acta*, 151: 99-108, 2015.
35. Amiri, M., Akbari Javar, H. and Mahmoudi-Moghaddam, H. Facile green synthesis of NiO/$NiCo_2O_4$ nanocomposite as an efficient electrochemical platform for determination of dopamine. *Electroanalysis*, 33(5):1205-1214, 2021.
36. Wei, Z., Guo, J., Qu, M., Guo, Z. and Zhang, H. Honeycombed-like nanosheet array composite $NiCo_2O_4$/rGO for efficient methanol electrooxidation and supercapacitors. *Electrochim. Acta*, 362:137145, 2020.

37. Gaskell, K.J., Starace, A. and Langell, M.A. $Zn_xNi_{1-x}O$ Rocksalt Oxide Surfaces: Novel Environment for Zn^{2+} and Its Effect on the NiO Band Structure. *J. Phys. Chem. C*, 111 (37):13912-13921, 2007.
38. Peck, M.A. and Langell, M.A. Comparison of nanoscaled and bulk NiO structural and environmental characteristics by XRD, XAFS, and XPS. *Chem. Mater*., 24 (23):4483-4490, 2012.
39. Chen, S., Huang, D., Liu, D., Sun, H., Yan, W., Wang, J., Dong, M., Tong, X. and Fan, W. Hollow and porous $NiCo_2O_4$ nanospheres for enhanced methanol oxidation reaction and oxygen reduction reaction by oxygen vacancies engineering. *Appl. Catal., B*, 291:120065, 2021.
40. Li, Z., Yang, R., Li, B., Yu, M., Li, D., Wang, H., Li, Q. Controllable synthesis of graphene/$NiCo_2O_4$ three-dimensional mesoporous electrocatalysts for efficient methanol oxidation reaction. *Electrochimica Acta*, 252:180–191, 2017.
41. Shen, J., Li, T., Long, Y., Shi, M., Li, N. and Ye, M. One-step solid state preparation of reduced graphene oxide. *Carbon*, 50 (6):2134-2140, 2012.
42. Stobinski, L., Lesiak, B., Malolepszy, A., Mazurkiewicz, M., Mierzwa, B., Zemek, J., Jiricek, P. and Bieloshapka, I. Graphene oxide and reduced graphene oxide studied by the XRD, TEM and electron spectroscopy methods. J. Electron Spectrosc. Relat. Phenom., 195:145-154, 2014.
43. Wang, W., Li, R., Zhang, R., Ma, J. and Wang, B. Electrocatalytic oxidation of methanol on glassy carbon electrode modified with nickel–manganese salen complexes encapsulated in mesoporous zeolite A. *J. Electroanal. Chem*., 742:110-121, 2015.
44. Samanta, S., Bhunia, K., Pradhan, D., Satpati, B. and Srivastava, R. $NiCuCo_2O_4$ supported Ni–Cu ion-exchanged mesoporous zeolite heteronano architecture: an efficient, stable, and economical nonprecious electrocatalyst for methanol oxidation. *ACS Sustainable Chem. Eng*., 6 (2):2023-2036, 2018.
45. Khadke, P., Tichter, T., Boettcher, T., Muench, F., Ensinger, W. and Roth, C. A simple and effective method for the accurate extraction of kinetic parameters using differential Tafel plots. *Scientific reports*, 11 (1):8974, 2021.
46. Hou, G., Parrondo, J., Ramani, V. and Prakash, J. Kinetic and mechanistic investigation of methanol oxidation on a smooth polycrystalline Pt surface. *J. Electrochem. Soc*., 161 (3):F252-F258 (2014).

47. Li, L. and Xing, Y. Methanol electro-oxidation on Pt-Ru alloy nanoparticles supported on carbon nanotubes. *Energies*, 2 (3):789-804, 2009.
48. Chaudhari, S., Bhattacharjya, D. and Yu, J.S. 1-Dimensional porous α-Fe_2O_3 nanorods as high performance electrode material for supercapacitors. *RSC Adv*., 3 (47):25120-25128, 2013.
49. Kawashima, A., Asami, K., Hashimoto, K., XPS analysis of amorphous Ni-Nb-Sn-Pt alloy catalysts for electrooxidation of formaldehyde. *Mater. Sci. Eng.: A* 134:1070-1073, 1991.
50. Bluhm, H., Hävecker, M., Knop-Gericke, A., Kleimenov, E., Schlögl, R., Teschner, D., Bukhtiyarov, V.I., Ogletree, D.F. and Salmeron, M. Methanol oxidation on a copper catalyst investigated using in situ X-ray photoelectron spectroscopy. *J. Phys. Chem. B*, 108 (38):14340-14347, 2004.
51. Vohs, J.M. and Barteau, M.A. Conversion of methanol, formaldehyde and formic acid on the polar faces of zinc oxide. *Surface science*, 176 (1-2):91-114, 1986.
52. Prosvirin, I.P., Tikhomirov, E.P., Sorokin, A.M., Kaichev, V.V. and Bukhtiyarov, V.I. In situ study of the selective oxidation of methanol to formaldehyde on copper. *Kinet. Catal*., 44:662-668, 2003.
53. Qiao, Z., Yang, X., Yang, S., Zhang, L. and Cao, B. 3D hierarchical MnO_2 nanorod/welded Ag-nanowire-network composites for high-performance supercapacitor electrodes. *Chem. Commun*., 52 (51):7998-8001, 2016.
54. Xia, H., Meng, Y.S., Li, X., Yuan, G. and Cui, C. Porous manganese oxide generated from lithiation/delithiation with improved electrochemical oxidation for supercapacitors. *J. Mater. Chem*., 21 (39):15521-15526, 2011.
55. da Rosa, C.G., Borges, C.D., Zambiazi, R.C., Nunes, M.R., Benvenutti, E.V., da Luz, S.R., D'Avila, R.F. and Rutz, J.K. Microencapsulation of gallic acid in chitosan, β-cyclodextrin and xanthan. Ind. Crops Prod., 46:138-146, 2013.
56. Wang, T., Turhan, M. and Gunasekaran, S. Selected properties of pH-sensitive, biodegradable chitosan–poly (vinyl alcohol) hydrogel. Polym Int., 53 (7):911-918, 2004.